PERGAMON

International Journal of Multiphase Flow 27 (2001) 2155–2187

International Journal of Multiphase Flow

www.elsevier.com/locate/ijmulflow

Modeling of dense gas–solid reactive mixtures applied to biomass pyrolysis in a fluidized bed

D. Lathouwers [a,1], J. Bellan [a,*]

[a] *Jet Propulsion Laboratory, Applied Technologies Section, California Institute of Technology, Mail Station 125-109, 4800 Oak Grove Drive, Pasadena, CA 91109, USA*

Received 23 March 2001; received in revised form 15 August 2001

Abstract

A model is presented for mathematically describing the thermofluid dynamics of dense, reactive, gas–solid mixtures. The model distinguishes among multiple particle classes, either on the basis of their physical properties (diameter, density) or through their thermochemistry (reactive versus inert particles). A multifluid approach is followed where macroscopic equations are derived from the kinetic theory of granular flows using inelastic rigid-sphere models, thereby accounting for collisional transfer in high-density regions. Separate transport equations are constructed for each of the particle classes, allowing for the description of the independent acceleration of the particles in each class and the interaction between size classes, as well as for the equilibration processes whereby momentum and energy are exchanged between the respective classes and the carrier gas. Aimed at high-density suspensions, such as fluidized beds, the relations obtained for the stress tensor are augmented by a model for frictional transfer, suitably extended to multiple-class systems. This model, previously derived, is here enlarged to include heat and mass transfer, as well as chemical reactions and is therefore applicable to general gas–solid combustion systems. The noteworthy novelties of the model with respect to other derivations in the literature include: (i) a systematic and consistent derivation of the solids transport equations and transport properties within the multifluid concept, allowing for non-equilibrium effects between the respective particle classes, (ii) the ability to explicitly account for the possibility of porous solid fuel particles, and (iii) the modeling of multiple chemical reactions in both gas and solid phases and the associated effects of heat and mass transfer. The model, which includes a separately validated chemistry model, is applied to high-temperature biomass particle pyrolysis in a lab-scale fluidized bed reactor and is used to obtain yield of reaction products. The results indicate that, at fixed initial particle size, the fluidizing gas temperature is the foremost parameter influencing tar yield. The biomass feed temperature, the nature of the feedstock, and the fluidization velocity all

* Corresponding author. Tel.: +1-818-354-6959; fax: +1-818-393-5011.

E-mail address: josette.bellan@jpl.nasa.gov (J. Bellan).

[1] Present address: Interfaculty Reactor Institute, Delft University of Technology, Mekelweg 15, 2629 JB Delft, Netherlands.

0301-9322/01/$ - see front matter
PII: S0301-9322(01)00059-3

have minor impact on the yield. It is also shown that the fluidizing gas temperature can be optimized for maximizing the tar yield.

1. Introduction

Many practical multiphase flow systems involve the flow of a dense, reactive, gas–particle mixture; 'dense' here refers to large particle volume fractions. Examples include coal combustion, catalyst regeneration and pyrolysis applications, among others. Because of the lack of fundamental knowledge of both the fluid-mechanical and thermal behavior of these systems, the design of these processes has been necessarily based on empirical correlations and experiments performed in laboratory- or pilot-scale units. However, detailed models and simulations of these systems would allow the optimization of the processes and their scaling, without needing expensive and time-consuming testing. The present investigation is the first step towards providing such a model.

One of the distinctive characteristics of dense particle flows is that momentum and energy are primarily exchanged through collisions between particles rather than through the gaseous phase (Savage and Sayed, 1984). The particles then interact similarly to the molecules of a dense gas. Jenkins and Savage (1983) first exploited this analogy and used a kinetic theory approach, based on Gaussian velocity distributions, to derive macroscopic equations of the mixture. Since then, this concept has been expanded and improved by considering more general velocity distributions (Lun et al., 1984; Jenkins and Richman, 1985), important for more dilute regions, and by including effects of the interstitial gas (e.g. Balzer et al., 1995), which may be important for small particles. A crucial role in these theories is played by the 'granular temperature', the third of the mean kinetic energy associated with the velocity fluctuations of the particles. Reviews on granular flows are given by Campbell (1990) and Goldhirsch (1999).

Most of the modeling work performed so far has focussed on isothermal, monodisperse mixtures. The majority of industrial interest, however, lies in systems that include multiple particle types and reactive flows, with their associated effects of mixing, segregation and heat transfer. Analyses of multicomponent dry granular mixtures are available (Farell et al., 1986; Jenkins and Mancini, 1987, 1989; Zamankhan, 1995), and are based on extensions of standard kinetic theory of dense gases (e.g. Tham and Gubbins, 1971), appropriately modified to include the effect of dissipation due to inelasticity. In all of the aforementioned references, equipartition of granular energy (the mean kinetic energy due to particle velocity fluctuations) of the respective particle classes is assumed. However, this assumption holds for molecular systems where dissipative effects are absent, and when the mass ratio of the respective particles is moderate. For granular flows, this assumption is inappropriate due to the dissipation associated with the inelasticity of particle collisions. Furthermore, all aforementioned studies assume the drift velocity between the respective particle classes to be small compared to a representative velocity of particle fluctuation, an assumption that is inappropriate for more dilute granular systems subject to body forces, causing appreciable drift (Gourdel et al., 1999).

The theoretical investigation of heat transfer in granular systems has been initiated only recently. Louge et al. (1993) investigated the thermal behavior of a dilute suspension whereas Hsiau (2000) has given a detailed analysis of the heat transfer coefficient for a wide range of particle fractions,

both for monodisperse and for binary mixtures. Theoretical foundations on dense, reactive multicomponent, mixtures, where all of the above processes play a role, are virtually absent in literature.

In the present study, we use a previously derived (Lathouwers and Bellan, 2000) comprehensive model for the isothermal flow of a multicomponent, dense, non-reactive, particle mixture to establish a general model including heat and mass transfer and chemical reactions; the hydrodynamic granular flow model has been validated using three separate sets of data from the literature. The separate dynamic equations derived for each particle class, describing the evolution of its mean velocity, temperature, etc., are now coupled through source terms that describe the various non-equilibrium processes, such as mass, momentum and energy transfer, both between particles and the gas, and between the respective particle classes. The kinetic theory is based on a Gaussian approximation for the velocity distribution, assuming the spatial gradients of the mean variables to be small and the particles to be nearly elastic. Detailed analysis of the heat transfer during a collision between particles indicates that this constitutes a negligible contribution, and consequently the conduction in the particle phases is treated as a self-diffusion phenomenon, based on the recent analysis given by Hsiau (2000). Other diffusive contributions, resulting from the random motion of the particles, are modeled in a similar way. The source terms expressing the transfer mechanisms are obtained by averaging the appropriate transfer correlations for a single particle.

As an application of the present work, the hydrodynamic equations are combined with a validated chemistry model for the description of biomass particle pyrolysis, consisting of seven solid species and two gaseous components. The complete model is then applied to the pyrolysis in a pilot-scale fluidized bed and specific product yields are calculated.

2. Mathematical model

A continuum model previously derived (Lathouwers and Bellan, 2000) for isothermal flows by applying separate averaging procedures for both the carrier gas and solid phases is here enlarged to include heat and mass transfer and chemical reactions. A phase ensemble average (carrier phase) is combined with a particle ensemble average; this procedure is attractive when resolution of the detailed internal-particle degrees of freedom (e.g. temperature or chemical composition profiles) is undesirable or unnecessary.

2.1. Single particle biomass pyrolysis model

The particle pyrolysis model employed here is that of Miller and Bellan (1997), based on superimposed cellulose, hemicellulose, and lignin reactions. This enables the simulation of different biomass feedstock through knowledge of the initial mass composition with respect to these three components; biomass impurities are lumped with the hemicellulose, as this model correlated best with the experimental data. Each of the virgin components undergoes the same generic competitive reaction scheme:

$$\begin{aligned} &\text{virgin (s)} \xrightarrow{K_1} \text{active (s)} \\ &\text{active (s)} \xrightarrow{K_2} \text{tar (g)} \xrightarrow{K_4} \text{gas (g)} \\ &\text{active (s)} \xrightarrow{K_3} X\text{char (s)} + (1-X)\text{gas (g)}. \end{aligned} \tag{1}$$

The virgin components, the active intermediates and the char are solid-phase species, while tar and gas are vapor products; these species are not pure chemical species but instead represent groups of compounds. All reactions are modeled with first-order Arrhenius kinetics,

$$K_i = A_i \exp(-E_i^a / R_u T), \tag{2}$$

where the rate constants, A_i, activation energies, E_i, for reactions K_1, K_2, K_3 and the mass ratio X are dependent on the particular component, whereas all heats of reaction and secondary tar decomposition parameters (K_4) are independent of the source component.

This kinetics model combined with a porous particle flow dynamics model yielded validated predictions on tar/char yields ranging from the kinetically controlled region (microparticles) to the diffusion controlled limit (macroparticles), c.f. Miller and Bellan (1997). Herein, the biomass pyrolysis is assumed kinetically controlled, which may be justified in the dense particulate regime where contact between particles may induce fragmentation (see Miller and Bellan, 1998, for a fragmentation model) and reduce the size of the particles to the point where the internal temperature equilibrates rapidly. Thus, the particle temperature, its mass and composition (global solid mass fractions) completely describe the state of the particle.

The sand and biomass particles are both solid and hence thermodynamically belong to the same phase. They, however, have different physical properties (e.g. the biomass particles are porous whereas the sand particles are not) and different temperatures, etc. Therefore these particle classes must be differentiated.

2.2. Gas-phase transport equations

As the procedure for phase ensemble averaging is well known (Drew, 1983), we will restrict the present discussion to the necessary results. The general ensemble average of a field quantity $\Psi(\mathbf{x}, t)$, ($\mathbf{x}, t$ denoting space and time coordinates) is

$$\langle \Psi(\mathbf{x}, t) \rangle = \int \Psi(\mathbf{x}, t) P(\Pi)\, \mathrm{d}\Pi, \tag{3}$$

where $P(\Pi)$ is the probability that a specific realization Π is encountered in the ensemble. The gas-phase ensemble average and its density-weighted counterpart are defined (Drew, 1983) as $\bar{\Psi} \equiv \langle \chi_g \Psi(\mathbf{x}, t) \rangle / \alpha_g$ and $\tilde{\Psi} \equiv \langle \chi_g \rho_g \Psi(\mathbf{x}, t) \rangle / \alpha_g \bar{\rho}_g$, where ρ_g is the gas density, χ_g denotes the phase indicator of the gas phase which is unity in the gas phase and zero otherwise, and the gas-phase fraction, α_g, is defined as the ensemble average of the indicator function, i.e. $\alpha_g = \langle \chi_g \rangle$. The average transport equations for the gas phase now follow by multiplying the local instantaneous equations (the Navier–Stokes set, supplemented with energy and species equations) by the phase indicator and then ensemble averaging:

$$\frac{\partial (\alpha \bar{\rho})_g}{\partial t} + \nabla \cdot (\alpha \bar{\rho} \tilde{\mathbf{u}})_g = \Gamma_g, \tag{4}$$

$$\frac{\partial (\alpha \bar{\rho} \tilde{\mathbf{u}})_g}{\partial t} + \nabla \cdot (\alpha \bar{\rho} \tilde{\mathbf{u}} \tilde{\mathbf{u}})_g = -\alpha_g \nabla \bar{p}_g + \nabla \cdot \alpha_g [\bar{\boldsymbol{\tau}} + \boldsymbol{\Sigma}^{\mathrm{Re}}]_g + \alpha_g \bar{\rho}_g \mathbf{f}_g + \mathbf{M}_g + \Gamma_g \mathbf{u}_g^i, \tag{5}$$

$$\frac{\partial(\alpha\bar{\rho}\tilde{h})_{\mathrm{g}}}{\partial t}+\nabla\cdot(\alpha\bar{\rho}\tilde{\mathbf{u}}\tilde{h})_{\mathrm{g}}=-\nabla\cdot\alpha_{\mathrm{g}}[\bar{\mathbf{q}}+\mathbf{q}^{\mathrm{Re}}]_{\mathrm{g}}+F_{\mathrm{g}}+\Gamma_{\mathrm{g}}h^{i}_{\mathrm{g}}, \tag{6}$$

$$\frac{\partial(\alpha\bar{\rho}\tilde{Y}_{\xi})_{\mathrm{g}}}{\partial t}+\nabla\cdot(\alpha\bar{\rho}\tilde{\mathbf{u}}\tilde{Y}_{\xi})_{\mathrm{g}}=-\nabla\cdot\alpha_{\mathrm{g}}[\bar{\mathbf{j}}_{\xi}+\mathbf{j}^{\mathrm{Re}}_{\xi}]_{\mathrm{g}}+\alpha_{\mathrm{g}}\bar{\rho}_{\mathrm{g}}\tilde{R}_{\mathrm{g}\xi}+H_{\mathrm{g}\xi}+\Gamma_{\mathrm{g}}Y^{i}_{\mathrm{g}\xi}. \tag{7}$$

Here, the main variables are the gas velocity $\mathbf{u}$, the specific enthalpy h, the gas thermodynamic pressure p_{g}, and the mass fractions of species ξ, Y_{ξ}. $\boldsymbol{\tau}$, $\mathbf{q}$, and $\mathbf{j}_{\xi}$ denote the molecular viscous stress, the molecular heat flux vector and the species diffusion flux vector, respectively. The gravitational acceleration is $\mathbf{f}_{\mathrm{g}}$, and $R_{\mathrm{g}\xi}$ is the reaction rate for species ξ. The terms $\mathbf{M}_{\mathrm{g}}$, F_{g}, and $H_{\mathrm{g}\xi}$ denote the diffusive interfacial transfer of momentum, enthalpy and species mass, respectively, and are defined in terms of the indicator function, e.g. $H_{\mathrm{g}\xi}\equiv\langle\mathbf{j}_{\mathrm{g}\xi}\cdot\nabla\chi_{\mathrm{g}}\rangle$. The terms Γ_{g}, $\Gamma_{\mathrm{g}}\mathbf{u}^{i}_{\mathrm{g}}$, $\Gamma_{\mathrm{g}}Y^{i}_{\mathrm{g}\xi}$, and $\Gamma_{\mathrm{g}}h^{i}_{\mathrm{g}}$ are the convective interfacial transfer fluxes of mass, momentum, enthalpy and species mass, and are expressed in terms of the gas velocity at the interface between the phases, $\mathbf{u}_{\mathrm{g}i}$, e.g. $\Gamma_{\mathrm{g}}\equiv\langle\rho_{\mathrm{g}}(\mathbf{u}_{\mathrm{g}}-\mathbf{u}_{\mathrm{g}i})\cdot\nabla\chi_{\mathrm{g}}\rangle$. Finally, the equations contain 'turbulent' fluxes, $\boldsymbol{\Sigma}^{\mathrm{Re}}_{\mathrm{g}}$, $\mathbf{j}^{\mathrm{Re}}_{\mathrm{g}\xi}$, $\mathbf{q}^{\mathrm{Re}}_{\mathrm{g}}$ expressing the flux of momentum, enthalpy and species mass given by e.g. $\alpha_{\mathrm{g}}\boldsymbol{\Sigma}^{\mathrm{Re}}_{\mathrm{g}}\equiv-\langle\chi_{\mathrm{g}}\rho_{\mathrm{g}}\mathbf{u}'_{\mathrm{g}}\mathbf{u}'_{\mathrm{g}}\rangle$, where the fluctuations result from a decomposition of each of the instantaneous variables into its mean and a fluctuation. In the above enthalpy equation, we have neglected the effect of pressure work and viscous dissipation.

Neglecting correlations between the gas temperature and mass fractions gives the averaged equation of state $\bar{p}_{\mathrm{g}}=R_{\mathrm{u}}\bar{\rho}_{\mathrm{g}}\sum_{\xi}(\tilde{Y}_{\xi}/W_{\xi})\tilde{T}_{\mathrm{g}}$, where R_{u} denotes the universal gas constant, W_{ξ} is the molecular weight of species ξ, and T_{g} is the gas thermodynamic temperature.

The average viscous stress tensor is approximated by a form similar to its microscopic counterpart, $\bar{\boldsymbol{\tau}}_{\mathrm{g}}=2\mu_{\mathrm{g}}\mathbf{S}_{\mathrm{g}}$, where $\mathbf{S}_{\mathrm{g}}$ denotes the strain rate tensor: $\mathbf{S}_{\mathrm{g}}=(\nabla\tilde{\mathbf{u}}_{\mathrm{g}}+\nabla\tilde{\mathbf{u}}^{\mathrm{T}}_{\mathrm{g}})/2-(\nabla\cdot\tilde{\mathbf{u}}_{\mathrm{g}})/3$ and μ_{g} is the gas viscosity. The average species flux $\bar{\mathbf{j}}_{\xi}$ is written as a simple gradient diffusion (Fickian) relation, neglecting multicomponent diffusion aspects: $\bar{\mathbf{j}}_{\xi}=-\bar{\rho}_{\mathrm{g}}\mathscr{D}_{\xi}\nabla\tilde{Y}_{\xi}$, where $\mathscr{D}_{\xi}$ is the mass diffusion coefficient. Similarly, the average molecular heat flux $\bar{\mathbf{q}}_{\mathrm{g}}$ is modeled in analogy with its molecular counterpart: $\bar{\mathbf{q}}_{\mathrm{g}}=-\lambda_{\mathrm{g}}\nabla\tilde{T}_{\mathrm{g}}-\sum_{\xi}h_{\xi}\bar{\mathbf{j}}_{\xi}$, with λ_{g} denoting the thermal conductivity coefficient, and where the second term represents the effect of species interdiffusion.

2.3. Particle-phase transport equations

The transport equations are derived similarly to those for dense gases, using kinetic theory concepts. Important differences from classical kinetic theory are the inelasticity of collisions between macroscopic particles leading to dissipation, and the presence of an interstitial gas exerting drag on the particles, which leads to interaction terms in the averaged transport equations.

While a considerable literature exists on the development of equations of motion for multicomponent mixtures, most of it is restricted to the case where the temperatures and velocities of the species are nearly equal and evolve according to the dynamic equations of the mixture. This classical mixture theory (Chapman and Cowling, 1970) requires that $\Delta u/\Theta_{\mathrm{c}}\ll 1$ (Δu being a characteristic relative velocity of the particle classes and Θ_{c} a characteristic rms velocity, related to a temperature in the molecular context). Furthermore, granular energy is assumed to be partitioned among the various particle classes according to their mass ratios (equipartition),

which may be inappropriate for granular flows due to the inelasticity of collisions. Therefore, here we derive separate dynamic equations for each of the particle classes, similar to those of Goldman and Sirovich (1967) for a dilute mixture of interacting species, c.f. Valiveti and Koch (1998).

Let $f_i^{(1)}(\mathbf{x}, \mathbf{c}, Y_\xi, T, m, t)$ denote the single-particle distribution function of particle class i such that $f_i^{(1)}$ is the probable number of particles of class i having their center of mass in the region $[\mathbf{x}, \mathbf{x} + \mathrm{d}\mathbf{x}]$, a velocity in the region $[\mathbf{c}, \mathbf{c} + \mathrm{d}\mathbf{c}]$, mass in the region $[m, m + \mathrm{d}m]$, mass fractions in $[Y_\xi, Y_\xi + \mathrm{d}Y_\xi]$, and temperature in $[T, T + \mathrm{d}T]$.

The number density, n_i, of particle phase i follows by integration of the single-particle distribution function f_i over all of phase space:

$$n_i(\mathbf{x}, t) = \int f_i \, \mathrm{d}\mathbf{c} \, \mathrm{d}Y_\xi \, \mathrm{d}T \, \mathrm{d}m. \tag{8}$$

With the previously derived single-particle distribution, a particle average is introduced:

$$\bar{\Psi}_i(\mathbf{x}, t) = \frac{1}{n_i} \int \Psi_i f_i \, \mathrm{d}\mathbf{c} \, \mathrm{d}Y_\xi \, \mathrm{d}T \, \mathrm{d}m. \tag{9}$$

The mass of the particles need not be uniform or constant with time, and therefore mass-weighted averages are also introduced:

$$\tilde{\Psi}_i(\mathbf{x}, t) = \frac{1}{\alpha_i \bar{\rho}_i} \int m_i \Psi_i f_i \, \mathrm{d}\mathbf{c} \, \mathrm{d}Y_\xi \, \mathrm{d}T \, \mathrm{d}m, \tag{10}$$

where

$$\alpha_i \bar{\rho}_i = n_i \bar{m}_i = \int m_i f_i \, \mathrm{d}\mathbf{c} \, \mathrm{d}Y_\xi \, \mathrm{d}T \, \mathrm{d}m. \tag{11}$$

This definition of the mass-weighted particle average is completely comparable to that used for the carrier phase and leads to more convenient forms of the moment equations, derived below. In the above expressions, α_i denotes the local phase fraction of class i (where pores are excluded) and $\bar{\rho}_i$ its corresponding average particle density. We also introduce equivalent definitions for $\hat{\alpha}_i$ and $\hat{\rho}_i$, where the pores of the particles are counted as volume belonging to the particle. Note that $\alpha_i \bar{\rho}_i = \hat{\alpha}_i \hat{\rho}_i$. Mass-weighted averages are also denoted by brackets, i.e. $\langle \Psi \rangle_i \equiv \tilde{\Psi}_i$ in the derivation below. Furthermore, we define the average velocity $\mathbf{u}_i = \langle \mathbf{c}_i \rangle$, the fluctuation velocity component, $\mathbf{C}_i = \mathbf{c}_i - \mathbf{u}_i$, and the granular temperature, $\Theta_i = \frac{1}{3} \langle C_i^2 \rangle$. The solidity, $\eta = 1 - \epsilon$, where ϵ is the porosity of a particle, is defined as the ratio of the volume displaced by the particle and the volume displaced by the particle if its pores had been closed. The solidity is then $\eta_i = m_i / V_i \sum (Y_\xi / \rho_\xi)$, where V_i is the total volume of a particle (including its pores). Here we assume that the particle diameter stays constant throughout the pyrolysis, and that the porosity of the particle increases in time (Miller and Bellan, 1997). This assumption is correct when the particle does not break or erodes.

The moment equations are derived by multiplying the Boltzmann equation by a variable $m\Psi$ and integrating over phase space. The general transport equation obtained is

$$\frac{\partial \alpha_i \bar{\rho}_i \tilde{\Psi}_i}{\partial t} + \nabla \cdot (\alpha_i \bar{\rho}_i \langle \mathbf{c}_i \Psi_i \rangle) = \sum_{k=A,B} C_{ik}(m_i \Psi_i) + \alpha_i \bar{\rho}_i \left\langle \frac{\mathbf{F}_i}{m_i} \frac{\partial \Psi_i}{\partial \mathbf{c}_i} \right\rangle + \alpha_i \bar{\rho}_i \left\langle \frac{\mathrm{d}T_i}{\mathrm{d}t} \frac{\partial \Psi_i}{\partial T_i} \right\rangle + \alpha_i \bar{\rho}_i \times \sum_{\xi} \left\langle \frac{\mathrm{d}Y_{i\xi}}{\mathrm{d}t} \frac{\partial \Psi_i}{\partial Y_{i\xi}} \right\rangle + \alpha_i \bar{\rho}_i \left\langle \frac{\mathrm{d}m_i}{\mathrm{d}t} \left[\frac{\partial \Psi_i}{\partial m_i} + \frac{\Psi_i}{m_i} \right] \right\rangle, \tag{12}$$

where $C_i(m_i \Psi_i)$ is the mean collisional rate of change of particle property Ψ_i. It represents an integral over all possible (binary) collisions of the change in $m_i \Psi_i$ multiplied by the probability that such a collision occurs. Jenkins and Mancini (1987, 1989) show that this integral can be written as the sum of a source-like contribution and a flux term, representing transport by collisions:

$$C_{ik}(m_i \Psi_i) = \chi_{ik}(m_i \Psi_i) - \nabla \cdot \theta_{ik}(m_i \Psi_i). \tag{13}$$

2.3.1. Collision dynamics

As in Jenkins and Mancini (1987), we consider two particle classes, A and B, although the formalism is general. These particles are assumed perfectly smooth and spherical. Their respective masses and radii are m_A, m_B, σ_A, and σ_B. Consider a collision between particle 1 of class i and particle 2 of class k, where i and k may be A or B; prime superscripts are used to denote a state right after collision. Below we consider the conservation of momentum and energy (mass and species are trivial) during a collision between particle 1 and 2.

Momentum: Assuming exclusively binary collisions and perfectly spherical and smooth particles, the relationship between the velocities of the particles right before and after a collision of particle 1 of class i and particle 2 of class k is determined from the conservation of momentum and energy; see Chapman and Cowling (1970). Defining $\mathbf{g}$ as the relative velocity, $\mathbf{c}_1 - \mathbf{c}_2$, we assume $\mathbf{g}$ before and after collision to be related by $(\mathbf{g}' \cdot \mathbf{k}) = -e_{ik}(\mathbf{g} \cdot \mathbf{k})$, where $\mathbf{k}$ is the unit vector connecting particle 1 and 2 at the moment of contact and e_{ik} is the restitution coefficient, incorporating the effect of inelasticity on the collisions ($e_{ik} = 1$ for elastic encounters). Further, define the sum of the particle masses $m_{ik} = m_i + m_k$ and the reduced mass $M_i = m_i/m_{ik}$. The center-of-mass velocity, $\mathbf{c}_m$, is constant during a collision and is found from $\mathbf{c}_m = M_k \mathbf{c}_2 + M_i \mathbf{c}_1 = M_k \mathbf{c}_2' + M_i \mathbf{c}_1'$. Thus

$$\mathbf{c}_1' - \mathbf{c}_1 = -M_k(1 + e_{ik})(\mathbf{g} \cdot \mathbf{k})\mathbf{k}. \tag{14}$$

Energy: Sun and Chen (1988) presented a detailed analysis of the heat transfer between two colliding particles. Their theory is based on the analysis of the elastic deformation of the spheres as they contact, and the resulting heat conduction. Following Sun and Chen (1988), the spheres have indices 1 and 2, and one defines the average radius, σ, the average mass, m, and the average elastic modulus, G, as

$$\sigma = \frac{\sigma_1 \sigma_2}{\sigma_1 + \sigma_2}; \qquad m = \frac{m_1 m_2}{m_1 + m_2}; \qquad G = \frac{4/3}{(1 - \nu_1^2)/G_1 + (1 - \nu_2^2)/G_2}, \tag{15}$$

where ν_i and G_i denote the Poisson ratios and the Young moduli of the respective materials. For small Fourier numbers for both spheres, based on the total contact time, t_c, and the contact area, A_c ($Fo = \pi a t_c / A_c$, with a the thermal diffusivity of the particle), the problem may be approximated by two contacting infinite plates, with the heat exchange given by

$$\Delta E = \frac{5.36(m/G)^{3/5}(\sigma g)^{7/10}(T_1 - T_2)}{(\rho C_p \lambda)_1^{-1/2} + (\rho C_p \lambda)_2^{-1/2}}, \tag{16}$$

where C_p is the heat capacity at constant pressure, g denotes the magnitude of $\mathbf{g}$, and the numerical constant is obtained from numerical integration. Sun and Chen (1988) note that $Fo \ll 1$ is valid if the velocity at which the particles collide is not too small ($\simeq$1 cm/s for sand).

2.3.2. Particle dynamics

The second component needed for the derivation of the moment equations is the rate of change of the particle properties along its trajectory.

Species mass fractions: As outlined earlier, the mass conversion rates are linear in the mass of the particle itself. In general we may write

$$\frac{\mathrm{d}m_{i,\xi}}{\mathrm{d}t} = \frac{\mathrm{d}(m_i Y_{i,\xi})}{\mathrm{d}t} = m_i R_{i,\xi}, \tag{17}$$

where $R_{i,\xi}$ represents the total rate, and may be the sum of several reactions involving the same component. The rate is linear in $Y_{i,\xi}$ and exponential in the particle temperature, as in Eq. 2.

Particle mass: The rate of change of the particle mass is obtained by summing the individual species rates

$$\frac{\mathrm{d}m_i}{\mathrm{d}t} = \sum_\xi \frac{\mathrm{d}m_{i,\xi}}{\mathrm{d}t} = m_i \sum_\xi R_{i,\xi}. \tag{18}$$

In practice, only some reactions contribute to phase change.

Momentum: The momentum equation of a single particle can be approximated as

$$m_i \frac{\mathrm{d}\mathbf{c}_i}{\mathrm{d}t} = \mathbf{F}_i = m_i \mathbf{f}_\mathrm{g} - V_i \nabla \overleftrightarrow{p}_\mathrm{g} + \frac{m_i}{\tau_{i,12}} (\overleftrightarrow{\mathbf{u}}_\mathrm{g} - \mathbf{c}_i), \tag{19}$$

where the total force on the particle is due to $\mathbf{f}_\mathrm{g}$, the gas pressure gradient and gas–particle drag. $V_i = \pi d_i^3/6$ and $\tau_{i,12}$ represents the relaxation time scale of the particle. The $\overleftrightarrow{(\,)}$ on the gas-phase variables denotes the evaluation of the variable at the location of the particle, as if the surrounding flow was undisturbed by its presence (Balzer et al., 1995). The gas–particle interaction time scale depends strongly on the flow regime; in the dilute regime it is derived from the drag coefficient, C_d, of a single particle in an infinite medium, empirically corrected for the presence of other surrounding particles by a function $f(\hat{\alpha}_\mathrm{g}) = \hat{\alpha}_\mathrm{g}^{-1.7}$ (e.g. Gidaspow, 1986), whereas in the dense regime the classical Ergun relation is used. To avoid discontinuous behavior, a weighted average of the two time scales is introduced:

$$\frac{1}{\tau_{i,12}} = W \frac{3\bar{\rho}_\mathrm{g} C_\mathrm{d}(Re_i)}{4\hat{\rho}_i d_i} |\mathbf{c}_i - \overleftrightarrow{\mathbf{u}}_\mathrm{g}| f(\hat{\alpha}_\mathrm{g}) + (1 - W) \frac{\bar{\rho}_\mathrm{g}}{\hat{\rho}_i} \left[(1 - \hat{\alpha}_\mathrm{g}) \frac{150}{Re_i} + 1.75 \right] \frac{|\mathbf{c}_i - \overleftrightarrow{\mathbf{u}}_\mathrm{g}|}{d_i}, \tag{20}$$

where the present switch function, $W(\hat{\alpha}_\mathrm{g}) = \arctan(150(\hat{\alpha}_\mathrm{g} - 0.8))/\pi + 1/2$, gives a rapid transition from one regime to the other. d_i is the diameter of the particle and Re_i is the Reynolds number based on the relative velocity with the gas, $Re_i = \hat{\alpha}_\mathrm{g} \bar{\rho}_\mathrm{g} |\mathbf{c}_i - \overleftrightarrow{\mathbf{u}}_\mathrm{g}| d_i / \mu_\mathrm{g}$. The single-particle drag coefficient C_d is determined from the well-known correlation (Schiller and Nauman, 1935) $C_\mathrm{d} = (24/Re_i)(1 + 0.15 Re_i^{0.687})$. Although not attempted in the present work due to the different

range in Re_i, this correlation may be further improved by adding a correction which results from the effect of mass transfer, as done in the validated model of Miller et al. (1999).

Energy: The rate of change of the particle's internal energy is due to heat exchange with the surrounding gas resulting from convection and diffusion, Q_{cd}, thermal radiation, Q_r, loss of vapor components to the gaseous phase carrying a specific enthalpy, h_v, and expansion work performed against the gas phase

$$m_i \frac{\mathrm{d}h_i}{\mathrm{d}t} = Q_{cd,i} + Q_{r,i} + \frac{\mathrm{d}m_i}{\mathrm{d}t}(h_v - h_i) + \frac{m_i}{\rho_i}\frac{\mathrm{d}p_g}{\mathrm{d}t}. \tag{21}$$

Here, the particle specific enthalpy, h_i, is defined as $h_i = \sum Y_{i,\xi} h_{i,\xi}$ and the average density of the particle is related to the 'true' densities of the individual solid species by $1/\rho_i = \sum Y_{i,\xi}/\rho_{i,\xi}$. The above equation can also be written in terms of the particle temperature, T_i, by using the thermodynamic differential for the specific enthalpy of a component: $\mathrm{d}h_{i,\xi} = C_{p,i,\xi}\mathrm{d}T_i + \mathrm{d}p_g/\rho_{i,\xi}$, where the pressure inside the particle has been equated to the gas pressure outside the particle. Using this relationship in Eq. 21 leads to the expected result

$$(mC_p)_i \frac{\mathrm{d}T_i}{\mathrm{d}t} = Q_{cd,i} + Q_{r,i} + \sum \frac{\mathrm{d}m_{i,\xi}}{\mathrm{d}t}(h_v - h_\xi), \tag{22}$$

where the effect of pressure has canceled, as it should. The last term on the right-hand side is exactly equal to the total heat of reaction for the particle.

The combined effect of convective and conductive heat transfer can be written in terms of an appropriate Nusselt relation $Q_{cd,i} = -\lambda_g \pi d_i Nu_i (T_i - \overleftrightarrow{T}_g)$, where Nu_i depends on the Re_i and on the Prandtl number, Pr_g, of the carrier gas. In obtaining relevant Nusselt relations for this situation, it is assumed that the particle temperature is uniform, i.e. the resistance to heat transfer is mainly in the gas phase. This assumption is consistent with those used to derive the continuum theory, as the state variables of the particles include their mean temperature only, i.e. no information on the internal temperature distribution is available. Implicitly, the Biot numbers are assumed small ($Bi = h_i' d_i/\lambda_i$, where h_i' is the gas–particle heat transfer coefficient). In the present case, the Nusselt number is taken as the single-particle Nusselt relation, multiplied by a correction blowing factor, F_{bl}, accounting for the effect of mass transfer on the heat transfer rate, i.e. $Nu = Nu_0 F_{bl}(Re_{bl}, Pr_g)$. The F_{bl} formulation used here is that of Miller et al. (1999), also given by Gyarmathy (1982), where the factor depends on the 'blowing Reynolds number', $Re_{bl} = \dot{m}/\pi d_i \mu_g$, as

$$F_{bl} = \frac{(Pr_g Re_{bl}/2)}{\mathrm{e}^{(Pr_g Re_{bl}/2)} - 1}. \tag{23}$$

For Nu_0, we use the standard Ranz correlation, $Nu_0 = 2 + 0.66 Re_i^{1/2} Pr_g^{1/3}$.

2.3.3. The moment equations

By making specific choices for Ψ in the transport theorem, specific moment equations are recovered.

Mass: The mass conservation equations are recovered by taking $\Psi = 1$:

$$\frac{\partial(\alpha_i \bar{\rho}_i)}{\partial t} + \nabla \cdot (\alpha_i \bar{\rho}_i \mathbf{u}_i) = \Gamma_i, \tag{24}$$

where the mass transfer

$$\Gamma_i = \alpha_i \bar{\rho}_i \left\langle \frac{1}{m_i} \frac{\mathrm{d}m_i}{\mathrm{d}t} \right\rangle = \alpha_i \bar{\rho}_i \sum_{\xi} \langle R_{i,\xi} \rangle$$

can be coupled to the conversion rate of solid- to gas-phase reactions.

Momentum: The momentum equations are generated using $\Psi = \mathbf{c}$:

$$\frac{\partial(\alpha_i \bar{\rho}_i \mathbf{u}_i)}{\partial t} + \nabla \cdot (\alpha_i \bar{\rho}_i \mathbf{u}_i \mathbf{u}_i) = \alpha_i \bar{\rho}_i \left\langle \frac{\mathbf{F}_i}{m_i} \right\rangle + \alpha_i \bar{\rho}_i \left\langle \frac{\mathrm{d}m_i}{\mathrm{d}t} \frac{\mathbf{c}_i}{m_i} \right\rangle - \nabla \cdot \boldsymbol{\Sigma}_i + \boldsymbol{\phi}_i, \tag{25}$$

where $\boldsymbol{\Sigma}_i = \alpha_i \bar{\rho}_i \langle \mathbf{C}_i \mathbf{C}_i \rangle + \sum_{k=A,B} \theta_{ik} (m_i \mathbf{C}_i)$ and $\boldsymbol{\phi}_i = \sum_{k=A,B} \chi_{ik} (m_i \mathbf{C}_i)$. The first term on the right-hand side of Eq. 25 is the average force exerted on the particle by the surrounding gas; the second represents the effect of mass transfer. The effective stress tensor $\boldsymbol{\Sigma}_i$ consists of a kinetic part and a collisional part that incorporates both effects from collisions between same class particles and between unlike particles. The final term in the transport equation is a source, also composed of collisional contributions between like and unlike particles. However, as the total momentum of phase i is conserved in a collision between two particles of that phase, only unlike particle collisions contribute to this term; an equivalent term does not appear in single-class formulations.

Species mass fractions: Taking $\Psi = Y_\xi$ gives

$$\frac{\partial(\alpha_i \bar{\rho}_i \tilde{Y}_{i\xi})}{\partial t} + \nabla \cdot (\alpha_i \bar{\rho}_i \mathbf{u}_i \tilde{Y}_{i\xi}) = -\nabla \cdot (\alpha_i \bar{\rho}_i \langle \mathbf{C}_i Y'_{i\xi} \rangle) + \Gamma_{i\xi}. \tag{26}$$

The first term on the right-hand side denotes the turbulent transport of the mass fraction. The second term, $\Gamma_{i\xi} = \alpha_i \bar{\rho}_i \langle R_{i,\xi} \rangle$, is the average mass source arising from reaction. No collisional terms are present, as the mass fractions do not change during a collision.

Granular temperature: Choosing $\Psi = 1/2C^2$, one obtains

$$\frac{3}{2}\left[\frac{\partial(\alpha_i \bar{\rho}_i \Theta_i)}{\partial t} + \nabla \cdot (\alpha_i \bar{\rho}_i \mathbf{u}_i \Theta_i)\right] = -\boldsymbol{\Sigma}_i : \nabla \mathbf{u}_i - \nabla \cdot \mathbf{q}_i + \gamma_i + \alpha_i \bar{\rho}_i \left\langle \frac{\mathrm{d}m_i}{\mathrm{d}t} \frac{1/2C_i^2}{m_i} \right\rangle + \alpha_i \bar{\rho}_i \left\langle \frac{\mathbf{F}_i}{m_i} \cdot \mathbf{C}_i \right\rangle. \tag{27}$$

The first term on the right-hand side of Eq. 27 is the production of fluctuation kinetic energy due to shearing of the solid phase. $\mathbf{q}_i = \alpha_i \bar{\rho}_i \langle 1/2 C_i^2 \mathbf{C} \rangle + \sum_{k=A,B} \theta_{ik} (1/2 m_i C_i^2)$ is the average 'heat flux' both due to velocity fluctuations and through collisions. The source term, $\gamma_i = \sum_k \chi_{ik} (\frac{1}{2} m_i C_i^2)$, represents the effects of energy redistribution among particle classes and the dissipative effect of inelastic collisions. Similar to the momentum equation, the source term is composed of a sum over both particle classes. The effect of mass transfer is contained in the next-to-last term of Eq. 27. The final term, which may be either a source or sink, represents the coupling with the surrounding gas phase.

Energy: Choosing $\Psi = h$, one obtains

$$\frac{\partial(\alpha_i \bar{\rho}_i \tilde{h}_i)}{\partial t} + \nabla \cdot (\alpha_i \bar{\rho}_i \mathbf{u}_i \tilde{h}_i) = \alpha_i \bar{\rho}_i \left\langle \frac{Q_{\mathrm{cd},i} + Q_{\mathrm{r},i}}{m_i} \right\rangle + \alpha_i \bar{\rho}_i \left\langle \frac{1}{\rho_i} \frac{\mathrm{d}p_\mathrm{g}}{\mathrm{d}t} \right\rangle + \alpha_i \bar{\rho}_i \left\langle \frac{\mathrm{d}m_i}{\mathrm{d}t} \frac{h_\mathrm{v}}{m_i} \right\rangle - \nabla \cdot \alpha_i \bar{\rho}_i \langle \mathbf{C}_i h'_i \rangle. \tag{28}$$

Here, the terms on the right-hand side denote the mean heat transfer with the surroundings, expansion work performed against the gas, the effect of mean enthalpy carried by the vapors exiting the porous particle, and the 'turbulent' flux. From a detailed analysis of the collision terms, they were found to be negligible.

2.4. Closure

The above model describes a particle mixture in a gaseous carrier using conservation equations for mass, momentum energy and granular temperature of each solid class. These multiple-class equations describe the independent accelerations of the species, as well as momentum and energy exchange between solid classes. Moreover, these transport equations are valid even when Δu is of the same order as Θ_c, and when the granular temperatures do not obey the equipartition law. The above system of equations contains several correlations, and is therefore unclosed. These correlations are of several types: (i) collisional contributions to both transport and source terms, (ii) exchange terms between gas and solids, (iii) in-phase transport terms and transport properties.

In principle, the single-particle distribution functions are solutions of the Boltzmann equations; however, they are difficult to obtain in situations when the phase space includes many variables (mass fractions, temperature, etc.). Therefore, it is assumed that the velocity distribution function solution of the hydrodynamic problem can be obtained without incorporating the explicit effect of the thermochemistry. The hydrodynamic problem is then decoupled from the thermochemistry, and the velocity distributions may be obtained by similar techniques as are used in non-reactive flow, taking into account the mean evolution of, for instance, the particle mass. The single-particle distribution function is then

$$f_i^{(1)}(\mathbf{x}, \mathbf{c}_i, Y_{\xi,i}, m_i, T_i, t) = f_i^{(1)*}(\mathbf{x}, \mathbf{c}_i, t)\delta(m_i - \bar{m}_i)\delta(T_i - \tilde{T}_i)\sum_{\xi}\delta(Y_{\xi,i} - \tilde{Y}_{\xi,i}), \tag{29}$$

where $f_i^{(1)*}$ is commonly called the velocity distribution (the asterisk is omitted in subsequent use of $f_i^{(1)*}$), excluding the effect of particle mass, particle temperature, and species concentrations.

2.4.1. Collisional and kinetic contributions

A Maxwellian velocity distribution is assumed. This is a good approximation when the flow has small spatial gradients, the collisions are nearly elastic and the particles are sufficiently heavy (i.e. the time between collisions is much smaller than the particle relaxation time; the particle–fluid correlation is small). The integrals require specification of the radial distribution function at contact, $h_{ik}(\mathbf{r})$, accounting for the effects of excluded area and particle shielding on the spatial distribution of colliding pairs. The form of $h_{ik}(\mathbf{r})$ is that of Jenkins and Mancini (1987), slightly adjusted to prevent overpacking of the solids, $\alpha_{\max}$ being the maximum allowable $\hat{\alpha}$:

$$h_{ik} = \frac{1}{1 - \hat{\alpha}/\alpha_{\max}} + 6\frac{\sigma_i\sigma_k}{\sigma_i + \sigma_k}\frac{\xi}{(1 - \hat{\alpha}/\alpha_{\max})^2} + 8\left(\frac{\sigma_i\sigma_k}{\sigma_i + \sigma_k}\right)^2\frac{\xi}{(1 - \hat{\alpha}/\alpha_{\max})^3}, \tag{30}$$

where $\xi = 2\pi/3\sum n_i\sigma_i^2$. The present study is targeted towards dense systems where the drift between particle classes is small. In our context, using distributions where each particle class has its own mean velocity introduces unnecessary complexity. Therefore, for calculation simplicity the

collision integrals are approximated by assuming that the relative velocity, $\Delta\mathbf{u}_{ik} = \mathbf{u}_i - \mathbf{u}_k$, is small compared to $(\Theta_i + \Theta_k)^{1/2}$. This assumption is also the basis of the classic Enskog expansion where in addition the granular temperatures are assumed equilibrated, and should not affect the applicability of the equations for our purposes. Here, the effects of having particle class specific Θ_i is, however, fully retained, which is important in dissipative systems, leading to deviations from equipartition.

Manger (1996) assumed a distribution identical to ours in order to obtain closure for a binary mixture. Kumaran and Koch (1993a,b) considered a slightly more general velocity distribution, i.e. an anisotropic Gaussian, where a distinction is made between the direction of gravity and the direction perpendicular to it. Although slightly more general, their work was restricted to homogeneous flows and is difficult to extend to inhomogeneous flows. Gourdel et al. (1999) also used Gaussians, but allowed a large drift between particle classes, leading to a homogeneous flow theory suitable for the complete range of particle packing.

Using the above distributions and neglecting products of the spatial gradients, products of $(1 - e_{ik})$ with spatial gradients, and products of $\Delta\mathbf{u}_{ik}$ with the spatial gradients, yields the following constitutive equations:

$$\boldsymbol{\phi}_i = \sum_k F_{ik}\left\{\frac{4}{3}\sqrt{2\pi}(\Theta_i + \Theta_k)^{1/2}(\mathbf{u}_k - \mathbf{u}_i) + \frac{\pi}{3}\sigma_{ik}(\Theta_i + \Theta_k)\nabla \ln\frac{n_i}{n_k}\right\}, \tag{31}$$

$$\boldsymbol{\Sigma}_i = n_i m_i \Theta_i \mathbf{I} + \sum_k \left\{p_{ik}\mathbf{I} - \mu_i^{ik}\left[2\mathbf{S}_i + \frac{5}{3}\nabla\cdot\mathbf{u}_i\right] - \mu_i^{kk}[2\mathbf{S}_k + \frac{5}{3}\nabla\cdot\mathbf{u}_k]\right\}, \tag{32}$$

$$\mathbf{q}_i = \sum_k \left\{\kappa_i^{ik}\nabla\Theta_i + \kappa_i^{kk}\nabla\Theta_k\right\}, \tag{33}$$

$$\gamma_i = \sum_k -2\sqrt{2\pi}F_{ik}(\Theta_i + \Theta_k)^{1/2}\{2(M_i\Theta_i - M_k\Theta_k) + M_k(1 - e_{ik})(\Theta_i + \Theta_k)\}, \tag{34}$$

where $F_{ik} = n_i n_k m_i M_k (1 + e_{ik}) h_{ik}\sigma_{ik}^2$. The indices on the viscosities and conductivities are arranged as follows: the subscript i indicates the relevance for class i, the first superscript labels the pertinent velocity gradient, and the k superscript denotes the collisions with particles of class k. The pressure and transport coefficients are

$$p_{ik} = \frac{1}{3}\pi n_i n_k m_i M_k (1 + e_{ik}) h_{ik}\sigma_{ik}^3(\Theta_i + \Theta_k), \tag{35}$$

$$\mu_i^{ik} = \frac{1}{15}\sqrt{2\pi}n_i n_k m_i M_k^2 (1 + e_{ik}) h_{ik}\sigma_{ik}^4(\Theta_i + \Theta_k)^{3/2}/\Theta_i, \tag{36}$$

$$\mu_i^{kk} = \frac{1}{15}\sqrt{2\pi}n_i n_k m_k M_i^2 (1 + e_{ik}) h_{ik}\sigma_{ik}^4(\Theta_i + \Theta_k)^{3/2}/\Theta_k, \tag{37}$$

$$\kappa_i^{ik} = \frac{1}{3}\sqrt{2\pi}n_i n_k m_i M_k (1 + e_{ik}) h_{ik}\sigma_{ik}^4(\Theta_i + \Theta_k)^{1/2}(M_k\Theta_k/\Theta_i), \tag{38}$$

$$\kappa_i^{kk} = \frac{1}{3}\sqrt{2\pi}n_i n_k m_i M_k (1 + e_{ik}) h_{ik}\sigma_{ik}^4(\Theta_i + \Theta_k)^{1/2}(M_i\Theta_i/\Theta_k). \tag{39}$$

The terms in $\boldsymbol{\phi}_i$ represent solid–solid drag and ordinary diffusion, respectively (thermal diffusion has been neglected). The stress tensor depends on the shear rates of all solid classes where the

shear viscosities arise entirely from collisions, not from streaming; this is a result of the Gaussian approximation. Similar remarks hold for the heat flux vector. The shear rates of both phases are assumed equal (in accordance with the assumption of small drift) so that $\mu_i = \sum_k \mu_i^{ik} + \mu_i^{kk}$. A similar procedure has been used for the conductivity. This procedure greatly simplifies coding, as the resulting equations are only coupled through algebraic terms, i.e. not differential terms. Manger (1996) recently presented slightly more general closure relations with some additional complexity in the granular energy flux, and which account for thermal diffusion. These additions are not warranted herein, considering the added complexity of non-isothermal reactive flow.

2.4.2. Exchange terms

To close the formulation, we evaluate the particle-to/from-gas exchange terms.

Mass and species: The mass exchange terms in the mass and species equations are evaluated at the average temperature and mass fractions, i.e.

$$\Gamma_i = \alpha_i \bar{\rho}_i \sum_\xi \tilde{R}_{i,\xi}^{\mathrm{s}\to\mathrm{g}} = \alpha_i \bar{\rho}_i \sum_\xi R_{i,\xi}(\{\tilde{Y}\}, \widetilde{T}_i), \tag{40}$$

where $\{\tilde{Y}\}$ denotes any combination of the set of species mass fractions, and where only solid-to-gas reactions need to be considered. Although this procedure neglects correlations between particle temperature and the mass fractions, these approximations are not too strict since the reaction rates are first order with respect to the species, and therefore do not exhibit the stronger non-linearity normally associated with second- or higher-order reaction rates. For consistency between the solids and gas phase we require $\Gamma_\mathrm{g} = -\sum_i \Gamma_i$.

A similar approach is followed for the reactive source terms in the individual species mass fraction equations for both carrier gas and the solid classes. Thus, these are evaluated at the mean temperature and mass fractions $\alpha\bar{\rho}\tilde{R}_\xi = \alpha\bar{\rho}R_\xi(\{\tilde{Y}\}, \tilde{T})$. Interfacial species transfer occurs only for the tar and gas species. The combined terms $H_{\mathrm{g}\xi} + \Gamma_\mathrm{g} Y_{\mathrm{g}\xi}^i$ form a mass source for the species equations originating from the appropriate solid-to-gas phase reactions (see Section 2.1 for the kinetics) which is calculated from the mean particle temperature and mean solid-phase mass fractions:

$$H_{\mathrm{g}\xi} + \Gamma_\mathrm{g} Y_{\mathrm{g}\xi}^i = \sum_i \alpha_i \bar{\rho}_i R_{i,\xi}^{\mathrm{s}\to\mathrm{g}}(\{\tilde{Y}\}, \tilde{T}_i). \tag{41}$$

Enthalpy: The gas- and solid-phase enthalpy equations may be rewritten in non-conservative form:

$$(\alpha\bar{\rho}C_p)_\mathrm{g} \frac{\mathrm{D}_\mathrm{g}\tilde{T}_\mathrm{g}}{\mathrm{D}t} = -\nabla\cdot(\alpha\bar{\mathbf{q}})_\mathrm{g} + F_\mathrm{g} + \Gamma_\mathrm{g}(h_\mathrm{g}^i - \tilde{h}_\mathrm{g}), \tag{42}$$

$$(\alpha_i\bar{\rho}C_p)_i \frac{\mathrm{D}_i\tilde{T}_i}{\mathrm{D}t} = \alpha_i\bar{\rho}_i\left\langle \frac{Q_{\mathrm{cd},i} + Q_{\mathrm{r},i}}{m_i} \right\rangle - \nabla\cdot\alpha_i\bar{\rho}_i\langle \mathbf{C}_i h_i'\rangle + \alpha_i\bar{\rho}_i\left\langle \frac{\mathrm{d}m_i}{\mathrm{d}t}\frac{(h_\mathrm{v} - \tilde{h}_i)}{m_i} \right\rangle, \tag{43}$$

where the gas pressure derivative in the solid equations has canceled out. The last term in the solids equation is the average reaction heat of all particle reactions (including solid-to-gas conversions). The energy equation contains the interaction term $\alpha_i\bar{\rho}_i\langle Q_{\mathrm{cd},i}\rangle$ that accounts for the gas–particle heat transfer. The following closure is provided for this term:

$$\alpha_i\bar{\rho}_i\left\langle\frac{Q_{\mathrm{cd},i}}{m_i}\right\rangle=-\frac{6\hat{\alpha}_i\lambda_{\mathrm{g}}}{d_i^2}\langle Nu_i\rangle(\tilde{T}_i-\tilde{T}_{\mathrm{g}}),\tag{44}$$

where $\langle Nu_i\rangle$ is calculated from the mean slip velocity etc. Although Louge et al. (1993) have incorporated the effect of particle velocity fluctuations on Nu, considering the complexity of the present problem including porous particles, heat transfer and chemical reactions, such an approach is not pursued here. The enthalpy flux associated with the vapor exiting the particle (tar and gas), $\sum_i \alpha_i\bar{\rho}_i\langle(\mathrm{d}m_i/\mathrm{d}t)(h_{\mathrm{v}}/m_i)\rangle$, requires knowledge of the specific enthalpies of the respective components. Such detailed properties are here unknown since many components are lumped together into pseudo-components referred to as gas and tar. This enthalpy flux is only needed for the gas phase, as the vapor enthalpy term is part of the total heat of reaction for the solids. To obtain closure, the differences in the formation enthalpies between the gas and the exiting vapors are neglected. We then obtain final closure of the gas-phase equation

$$\begin{aligned}F_{\mathrm{g}}+\Gamma_{\mathrm{g}}(h_{\mathrm{g}}^i-\tilde{h}_{\mathrm{g}})=&\sum_i\frac{6\hat{\alpha}_i\lambda_{\mathrm{g}}}{d_i^2}\langle Nu\rangle_i(\tilde{T}_i-\tilde{T}_{\mathrm{g}})+\sum_i\Gamma_{\mathrm{tar}}^{\mathrm{s}\to\mathrm{g}}(C_p^{\mathrm{tar}}\tilde{T}_{\mathrm{b}}-C_{p,\mathrm{g}}\tilde{T}_{\mathrm{g}})\\&+\Gamma_{\mathrm{gas}}^{\mathrm{s}\to\mathrm{g}}(C_p^{\mathrm{gas}}\tilde{T}_i-C_{p,\mathrm{g}}\tilde{T}_{\mathrm{g}}),\end{aligned}\tag{45}$$

where we have further assumed that the vapor products are leaving the particle at its mean temperature, and where $\Gamma_{\mathrm{tar}}^{\mathrm{s}\to\mathrm{g}}$, and $\Gamma_{\mathrm{gas}}^{\mathrm{s}\to\mathrm{g}}$ denote the averaged mass transfer rates of, respectively, tar and gas. The thermal radiation term, $\alpha_i\bar{\rho}_i\langle Q_{\mathrm{r},i}/m_i\rangle$, is modeled below.

Momentum: The mass transfer related term is modeled using a mean value approximation, i.e.

$$\Gamma_{\mathrm{g}}\mathbf{u}_{\mathrm{g}}^i=\sum_i\left\langle\frac{\mathrm{d}m_i}{\mathrm{d}t}\frac{\mathbf{c}_i}{m_i}\right\rangle=\sum_i\Gamma_i\tilde{\mathbf{u}}_i.\tag{46}$$

Hence, the average interfacial gas velocity is approximated by the mean velocity of the particle class responsible for the mass transfer. The interaction term in the momentum equation may be expanded to

$$\alpha_i\bar{\rho}_i\left\langle\frac{\mathbf{F}_i}{m_i}\right\rangle=\alpha_i\bar{\rho}_i\left[\mathbf{f}_{\mathrm{g}}-\left\langle\frac{V_{\mathrm{p}}}{m_i}\nabla\overleftrightarrow{p}_{\mathrm{g}}\right\rangle-\left\langle\frac{1}{\tau_{i,12}}(\mathbf{c}_i-\overleftrightarrow{\mathbf{u}}_{\mathrm{g}})\right\rangle\right].\tag{47}$$

The pressure gradient term is closed in terms of the mean gas pressure gradient:

$$-\alpha_i\bar{\rho}_i\left\langle\frac{V_{\mathrm{p}}}{m_i}\nabla\overleftrightarrow{p}_{\mathrm{g}}\right\rangle\approx-\hat{\alpha}_i\nabla\bar{p}_{\mathrm{g}}.\tag{48}$$

Similarly, for the drag force related term:

$$-\alpha_i\bar{\rho}_i\left\langle\frac{1}{\tau_{i,12}}(\mathbf{c}_i-\overleftrightarrow{\mathbf{u}}_{\mathrm{g}})\right\rangle\approx-\frac{\alpha_i\bar{\rho}_i}{\tau_{i,12}}(\mathbf{u}_i-\langle\overleftrightarrow{\mathbf{u}}_{\mathrm{g}}\rangle_i),\tag{49}$$

where fluctuations in the particle relaxation time are neglected. The particle average of the locally undisturbed velocity is set equal to the phase-averaged velocity: $\langle\overleftrightarrow{\mathbf{u}}_{\mathrm{g}}\rangle\approx\tilde{\mathbf{u}}_{\mathrm{g}}$. For consistency between the gas and solids equations, $\mathbf{M}_{\mathrm{g}}=\sum_i(\alpha_i\bar{\rho}_i/\tau_{i,12})(\mathbf{u}_i-\tilde{\mathbf{u}}_{\mathrm{g}})$.

Granular energy: Two terms require closure, the mass transfer related correlation and the term related to the presence of an interstitial gas. The transfer term is closed assuming that fluctuations

in the granular temperature are negligible, i.e.

$$\alpha_i\bar{\rho}_i\left\langle \frac{\mathrm{d}m_i}{\mathrm{d}t}\frac{1/2C_i^2}{m_i}\right\rangle = \frac{3}{2}\Gamma_i\Theta_i. \tag{50}$$

The interaction term with the gas phase can be expanded as

$$\alpha_i\bar{\rho}_i\left\langle \frac{\mathbf{F}_i}{m_i}\cdot\mathbf{C}_i'\right\rangle = \frac{\alpha_i\bar{\rho}_i}{\tau_{i,12}}(\langle\mathbf{C}_i'\cdot\mathbf{u}_{\mathrm{g}}''\rangle_i - \langle\mathbf{C}_i'\cdot\mathbf{C}_i'\rangle_i), \tag{51}$$

where gas pressure gradient fluctuations have been neglected and we have decomposed the undisturbed gas velocity in a mean value at the particle location and a fluctuation $\overleftrightarrow{\mathbf{u}}_{\mathrm{g}} = \langle\overleftrightarrow{\mathbf{u}}_{\mathrm{g}}\rangle_i + \mathbf{u}_{\mathrm{g}}''$. For large particles having large particle–fluid interaction time compared to the time between collisions, the term represented by Eq. 51 may be neglected (dry granular mixture).

2.4.3. In-phase transport fluxes and evaluation of transport properties

Much of the transport closure used for the gas phase has already been discussed in the context of gas-phase averaging. Here we focus on the solid-phase closure. The in-phase transport fluxes for the solid classes comprise the correlations between the velocity of the respective class and a variable, not explicitly considered in the distribution function, i.e. the species mass fractions, $Y_{i\xi}$, the particle mass, m, or the temperature T. These transport fluxes arise from the self-diffusive transport of the respective property, carried by the particles. In analogy with the work of Louge et al. (1993), these 'turbulent' fluxes are modeled using a self-diffusive coefficient, $\mathscr{D}_{ii}$, derived from the Gaussian velocity distribution

$$-\nabla\cdot(\alpha_i\bar{\rho}_i\langle\mathbf{C}_iY_{i\xi}'\rangle) = \nabla\cdot(\alpha_i\bar{\rho}_i\mathscr{D}_{ii}\nabla\tilde{Y}_{i\xi}), \tag{52}$$

$$-\nabla\cdot(\alpha_i\bar{\rho}_i\langle\mathbf{C}_ih_i'\rangle) = \nabla\cdot(\alpha_i\bar{\rho}_iC_{p,i}\mathscr{D}_{ii}\nabla\tilde{T}_i). \tag{53}$$

The derivation of $\mathscr{D}_{ii}$ is detailed in Appendix A and follows the recent work of Hsiau (2000).

2.4.4. Transport equations for the mean particle mass and solidity

The transport theorem, used for the particle mass, gives a transport equation for $\tilde{m}_i$, not $\bar{m}_i$; however, it is $\bar{m}_i$ that is required by the model for calculation of the average solidity and the collision terms. The approach used here is to equate the mass-weighted average to the non-weighted result, a procedure commonly practiced in work related to compressible single-phase turbulence. The following transport equation then follows:

$$\frac{\partial(\alpha\bar{\rho}\bar{m})_i}{\partial t} + \nabla\cdot(\alpha\bar{\rho}\mathbf{u}\bar{m})_i = \nabla\cdot\alpha_i\bar{\rho}_i\mathscr{D}_{ii}\nabla\bar{m}_i - 2\Gamma_i\bar{m}_i, \tag{54}$$

where turbulent diffusion has been included in a similar manner as in the energy and species equations. The average solidity is then derived from the average particle mass as $\bar{\eta}_i = \bar{m}_i/V_i\sum_\xi\tilde{Y}_\xi/\rho_\xi$.

2.5. Frictional transfer

The constitutive equations derived above are restricted to the volume fraction regime where particles interact exclusively through slightly inelastic, short-duration collisions. However, as the volumetric fraction approaches $\alpha_{\max}$, particles will, increasingly, be in simultaneous contact with several neighbors and stresses will be transmitted at points of sustained sliding or rolling contact. This situation is very difficult to model at the microscopic level, leading to its neglect in many bubbling fluidized bed models. However, in certain regions where shear rates are very small, Θ_i may be too small to support the solids phase. Hence, codes based on models neglecting friction require a 'numerical fix', generally restricting the value of the computed Θ_i. To avoid this situation, we explicitly model the frictional regime. The approach followed is similar to that used in Syamlal (1993), extended here for the case of multiple particle classes. The model proposed attains a simple relation between stresses and strains: $\mathbf{\Sigma}_i^{\mathrm{f}} = -p_i^{\mathrm{f}}\mathbf{I} + 2\mu_i^{\mathrm{f}}\mathbf{S}_i$ for $\alpha > \alpha_{\min}$, where $\alpha_{\min}$ is the minimum α at which frictional transfer becomes influential. Experimental observations indicate that the frictional normal stress increases rapidly with bulk density and diverges as $\alpha_{\max}$ is approached (Savage and Sayed, 1984). A simple algebraic representation of this behavior is (c.f. Anderson and Jackson, 1992)

$$p_i^{\mathrm{f}} = \frac{\alpha_i \bar{\rho}_i}{\sum \alpha_i \bar{\rho}_i} Fr \frac{(\hat{\alpha} - \alpha_{\min})^p}{(\alpha_{\max} - \hat{\alpha})^n}, \tag{55}$$

where Fr is a material constant. The frictional viscosity, μ_i^{f}, is related to the frictional pressure and the angle of internal friction, ϕ, as $\mu_i^{\mathrm{f}} = p_i^{\mathrm{f}} \sin(\phi)/2\sqrt{I_2}$ where I_2 denotes the second invariant of the strain rate tensor. The following values for the parameters have been used in the present simulations: $p = 2$, $n = 5$, $Fr = 0.005$, $\alpha_{\min} = 0.6$, $\alpha_{\max} = 0.64$, and $\phi = 25°$, which are in general agreement with those of Anderson and Jackson (1992).

Following Johnson and Jackson (1987), the total stress is taken as the sum of the contributions from the separate mechanisms, each evaluated as though it acted alone: $\mathbf{\Sigma}^{\mathrm{tot}} = \mathbf{\Sigma}^{\mathrm{f}} + \mathbf{\Sigma}^{\mathrm{c}}$. Here the superscript c indicates both collisional and kinetic contributions. However, in the production term of Eq. 27, the frictional terms are deleted, inherently assuming that the frictional work is directly converted to thermal internal energy.

2.6. Thermal radiation

Here, we have assumed the gas to be transparent, which is a good approximation at the relatively low gas temperatures. Therefore, to evaluate the radiative contribution in Eq. 43, the local radiation intensity needs to be calculated based on particle–particle exchanges. The radiation transfer equation for the radiation intensity $I(\mathbf{x}, \mathbf{s})$ at position $\mathbf{x}$ in direction $\mathbf{s}$ in an absorbing and scattering grey medium is

$$\mathbf{s} \cdot \nabla I(\mathbf{x}, \mathbf{s}) = -(\kappa_{\mathrm{a}} + \kappa_{\mathrm{s}}) I(\mathbf{x}, \mathbf{s}) + \kappa_{\mathrm{a}} I_{\mathrm{bb}} + \frac{\kappa_{\mathrm{s}}}{4\pi} \int_{4\pi} I(\mathbf{x}, \mathbf{s}') p_{\mathrm{s}}(\mathbf{s}', \mathbf{s}) \, \mathrm{d}\mathbf{s}'. \tag{56}$$

Here, κ_{a} and κ_{s} are the absorption and scattering coefficients of the medium, respectively. The integral term accounts for scattering of the two-phase medium (through the particles only) and $p_{\mathrm{s}}(\mathbf{s}', \mathbf{s})$ is the mixture phase function which is a function of the angle between the incoming ($\mathbf{s}'$)

and the scattered (**s**) radiation. This equation is approximately solved using the six-flux method (see e.g. Zaichik et al., 1997). As the present application is towards dense systems, scattering is expected to be isotropic. We therefore assume $p_s(\mathbf{s}', \mathbf{s}) = 1$, giving equal forward, backward and side-scattering ratios (equaling 1/6).

With the calculated radiative intensities, I_i, the sources in the thermal energy equations of the solids are given by

$$\alpha_i \bar{\rho}_i \left\langle \frac{Q_{r,i}}{m_i} \right\rangle = -4\pi\kappa_{ai}\left(I_{bbi} - \frac{I_x + I_y + I_z}{3}\right), \tag{57}$$

where the black-body radiation intensity for the mixture is calculated from the weighted (by the emissivities, i.e. absorptivities) sum of the individual intensities of the solids $I_{bb} = (1/\kappa_a)\sum_i \kappa_{ai} I_{bbi}$, with the black-body intensity for class i given by $I_{bbi} = \sigma_{Bo} T_i^4/\pi$, where σ_{Bo} is the Stefan–Boltzmann constant.

The absorptivity and scattering coefficients of the mixture are summed over all solid classes, $\kappa_a = \sum_i \kappa_{ai}$ and $\kappa_s = \sum_i \kappa_{si}$, where the individual absorptivities are given in terms of the volume fraction of the particles (not explicitly accounting for porosity) and the efficiency factors, Q, as determined by Mie theory as $\kappa_{ai} = 3Q_{ai}\hat{\alpha}_i/2d_i$ and $\kappa_{si} = 3Q_{si}\hat{\alpha}_i/2d_i$. In the limit of large particles, Mie theory asymptotes to geometric optics for which the efficiency factors equal 1, $Q_{ai} = Q_{si} = 1$.

2.7. Initial and boundary conditions

Initial conditions are specified corresponding to a fluid bed at rest: velocities of all phases are set to zero; the granular energy is set to a very small number, typically 10^{-7} m^2/s^2, and the volume fraction of the solid is set to 0.6, i.e. close to maximum packing of 0.64. To break the symmetry of the flow, i.e. to induce bubbling, several asymmetrically distributed void areas are created at the bottom of the bed. Although these regions consist of only a few number of grid cells, they are sufficient to induce the required asymmetry. Note that the effects of the initial conditions fade over time and do not affect the statistical behavior of the fluid flow.

Inflow conditions are specified to reflect realistic conditions corresponding to bubbling fluidization, i.e. at inlet sections, the volume fractions and velocities are specified together with the temperatures of all phases and the composition of the gas phase and biomass particles, depending on the pertinent feedstock used. The initial temperature of the sand and the gas in the domain is set equal to the inlet temperature of the fluidization gas. Hence, although initially the sand bed is stationary, it is assumed that the fluidization gas has preheated it. This does not affect the calculation of product yield, as we are interested in the asymptotic (i.e. after a statistically steady flow field has emerged) behavior of the reactor.

Along solid walls, no-slip conditions are applied for the gas phase ($\mathbf{u}_g = 0$), whereas the solids are allowed to slip freely ($\partial \mathbf{u}_{i,t}/\partial n = 0$, where n is a unit normal and the subscript t denotes tangential). Zero-flux boundary conditions are imposed for the solid thermal energy equations, consistent with the energy transfer in particle–wall collisions being negligible. As the thermal boundary layers along the wall are not resolved, a similar condition is imposed for the gas phase. For boundary conditions of the thermal radiation model we refer the reader to Zaichik et al. (1997).

At outlets, Neumann conditions are specified for all variables except for the velocity component normal to the outlet plane, which is calculated in a similar manner as in the interior of the domain using atmospheric pressure at the outlet plane ($p_g = 1$ atm.). Solids are inhibited to exit the computational domain, simulating a fine solids-filtering grid.

3. Solution procedure

Spatial discretization of the governing equations is based on a finite-volume technique using a staggered grid. All convective fluxes are approximated with a second-order-accurate bounded TVD scheme avoiding excessive numerical diffusion. The time discretization is based on a backward Euler scheme in combination with a pressure-correction technique. The momentum equations of all phases are solved in a coupled manner, though separately for each velocity direction. Compared with the well-known partial elimination algorithm (PEA) the present approach is more general (see Lathouwers, 1999, for more details on full-field coupling). The species and energy equations constitute a strongly coupled, stiff system of equations. To avoid very large linear systems arising from (the necessarily) implicit discretization, a time splitting is used for the combined species and energy system consisting of three steps: (i) performance of a half convection–diffusion time step, (ii) time integration of the equations over a full time step with only the source terms present (reaction terms, radiation, etc.), (iii) performance of another half convection–diffusion time step. The advantage of this split scheme is that, during steps (i) and (iii), the equations are decoupled into standard convection–diffusion systems which are easily handled, whereas in step (ii) there is no spatial coupling. The stiff integration in step (ii) is performed by the well-known stiff integrator VODE (Brown et al., 1989). All sparse linear systems arising from the discretization of convection–diffusion systems are solved with preconditioned Krylov methods (conjugate gradient (CG) for the pressure Poisson equation and Generalized Minimum RESidual (GMRES) for the other transport equations; see e.g. Barrett et al., 1994).

All computations are performed on a 40×148 uniform grid (x and y directions, respectively).

4. Results

In a previous paper (Lathouwers and Bellan, 2000), the isothermal model was applied to a variety of test cases in order to quantify its predictive capabilities by comparing with data available in the literature. These included (i) comparison of the stresses generated by the shearing of a homogeneous particle mixture (see Savage and Sayed, 1984), (ii) comparison of the particle pressure generated along the wall of a bubbling fluidized bed (see Campbell and Wang, 1991), (iii) the characteristic behavior of monodisperse and binary homogeneously fluidized beds (Johnsson et al., 1991). Comparisons performed with several sets of experiments validated the hydrodynamic aspect of the model. In contrast to the previous investigation which was devoted to isothermal situations, the present study explores biomass particle pyrolysis in a fluidized bed reactor.

Among the pyrolysis reactor designs investigated for commercial production of condensable tars from biomass, the fluidized bed reactor is potentially efficient due to the high particle heating rates that can be achieved (Scott et al., 1999) and its excellent mixing properties, assuring a

reasonably uniform product quality. A further interesting feature of this type of reactor is that char does not accumulate in the bed, but is elutriated with the gas flow instead, after which it may be filtered out, making the reactor very suitable for continuous operation.

The fluidized bed reactor contains a large amount of sand that is used as inert bed material which acts as heat capacitance for the biomass that is injected into the bed. Fluidization of the sand–biomass mixture is generally achieved by using either hot steam or nitrogen, some of which is also injected with the biomass, therefore preheating it. Once the particles enter the reactor, the temperature of the biomass rises rapidly and pyrolysis rates increase causing solid biomass species to be converted into tar and gas which are subsequently ejected from the particle, while char that is also formed in the process maintains the particle matrix. Biomass particle pyrolysis is an endothermic process and heat has to be supplied continuously by the surrounding gas, which in turn is heated by the sand. The gaseous reaction products are convected out of the reactor together with the fluidization gas to locations where they are subsequently cooled to prevent product degradation.

Although the process has received considerable attention experimentally (e.g. Scott and Piskorz, 1982, 1984), currently there are no thorough theoretical analyses available, addressing simultaneously all physico-chemical processes in the reactor. Most of the work to date has focused on single-particle pyrolysis in a gas stream, which requires a priori knowledge of ambient gas flow parameters, its temperature in particular (Miller and Bellan, 1997; Di Felice et al., 1999).

Below, we present quantitative results from numerical simulations based on the detailed mathematical model presented above.

4.1. Physico-chemical parameters of biomass pyrolysis

The kinetics scheme of the present biomass pyrolysis model was presented in Section 2. All values of A_i and E_i are tabulated in Table 1 (c.f. Miller and Bellan, 1997), and are dependent on the source component. Due to a lack of more detailed knowledge, the heats of reaction are taken as independent of the source component. The depolymerization reaction K_1 has $\Delta h_1 = 0$ kJ/kg, reaction K_2 is endothermic with $\Delta h_2 = 255$ kJ/kg, and both the char formation and the secondary

Table 1
Rate constants and activation energy for the biomass pyrolysis kinetics scheme (Eq. (1))

Reaction	A (1/s)	E (J/kmol)
K_1^c	2.8×10^{19}	242.4×10^6
K_2^c	3.28×10^{14}	196.5×10^6
K_3^c	1.30×10^{10}	150.5×10^6
K_1^h	2.10×10^{16}	186.7×10^6
K_2^h	8.75×10^{15}	202.4×10^6
K_3^h	2.60×10^{11}	145.7×10^6
K_1^l	9.60×10^8	107.6×10^6
K_2^l	1.50×10^9	143.8×10^6
K_3^l	7.70×10^6	111.4×10^6
K_4	4.28×10^6	108×10^6

The char formation ratios for reaction K_3 are: $X^c = 0.35$, $X^h = 0.60$, and $X^l = 0.75$.

tar reactions are exothermic with $\Delta h_3 = -20$ kJ/kg and $\Delta h_4 = -42$ kJ/kg. All other properties of gaseous and solid species are listed in Lathouwers and Bellan (2001).

4.2. Simulation conditions

A sketch of the simulated geometry and the boundary conditions employed is given in Fig. 1. The geometry has been chosen to resemble that used in experiments by Scott and Piskorz (1982, 1984), among others. Although the real fluidized bed is a cylindrical vessel, for computational simplicity, the present computational domain is approximated to be rectangular. In the simulations, the biomass is fed through an inlet section in one of the side walls, together with an amount of gas, which preheats the biomass during the feeding process. The center of feed-point 1 is located 4.6 cm from the bottom of the bed and has a height (area) of 1.86 cm; feeder no. 2 has the same height (area) and is located 12.1 cm from the bottom. In the present simulations, the temperature of the gas used for fluidization is equal to that fed through the biomass feed section (T_g); the inlet temperature of the biomass, however, is assumed to vary (T_b) to investigate the effect of preheating. Note that, regardless of the biomass feed temperature, the biomass compositions used at the inlet correspond to those of biomass that has not pyrolyzed, i.e. it is assumed that the residence time in the feeder is short (no appreciable biomass conversion) while the effective heating of the particles is as efficient as required (by specifying the required temperature). To vary the cellulose/hemicellulose/lignin proportions of the feedstock, bagasse, olive husk, maple, and oak are used in the simulations. The initial biomass composition of these biomass types are given in Table 2. The diameter of the sand and biomass particles is assumed 0.5 mm, which is a common value in practical operation, and is varied parametrically to explore its effect on tar yield. The biomass particles are assumed to have an initial porosity of 0.7 (c.f. Miller and Bellan, 1997). The biomass feed flux is constant and has a value of 0.5 kg/m^2 s (when two feed-points are used,

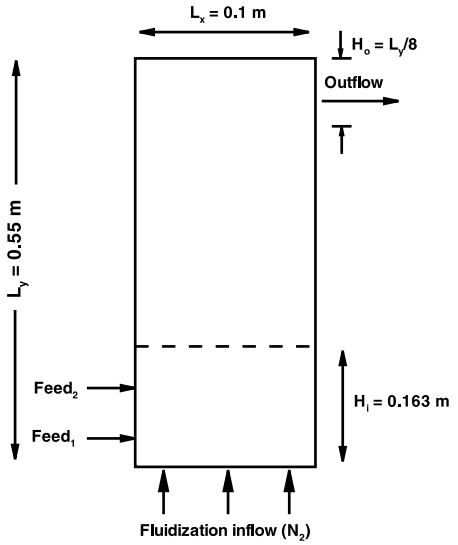

Fig. 1. Schematic of the fluidized bed.

Table 2
Initial biomass composition by mass fractions (cf. Miller and Bellan, 1997)

Feed	Cellulose	Hemicellulose	Lignin
Bagasse	0.36	0.47	0.17
Maple	0.40	0.38	0.22
Oak	0.35	0.40	0.25
Olive husk	0.22	0.33	0.45

the flow is equally split between feed-points). The gas velocity through the feeder is 0.5 m/s. The gas velocity used for fluidization of the mixture is varied from 0.5 to 0.7 m/s and is uniform over the bottom of the domain. A summary of all simulations performed is listed in Table 3. Initial conditions correspond to a bed filled with sand only up to a height of 0.163 m at a volume fraction of 0.6 which corresponds to dense packing.

4.3. Results and discussion

Regardless of the local phenomena in the reactor, the true measure of the reactor efficiency for the tar production can be quantitatively determined by comparing the actual mass of tar exiting the reactor (Ω_{tar}) and the amount still present in its interior (M_{tar}) to the biomass feed flow (M_{feed}):

$$\Omega_{\text{tar}} = \int_0^t \int_{\text{outlet}} (\alpha_g \bar{\rho}_g \tilde{\mathbf{u}}_g \tilde{Y}_{\text{tar}}) \, \mathrm{d}\mathbf{A} \, \mathrm{d}t', \tag{58}$$

Table 3
Summary of operating parameters in the simulations performed

Run no.	T_g (K)	T_b (K)	Feedpoint	Feedstock	Feed rate	V_g (m/s)	d_p (mm)
1	600	400	1	Bagasse	1	0.5	0.5
2	700	400	1	Bagasse	1	0.5	0.5
3[a]	750	400	1	Bagasse	1	0.5	0.5
4	800	400	1	Bagasse	1	0.5	0.5
5	850	400	1	Bagasse	1	0.5	0.5
6	950	400	1	Bagasse	1	0.5	0.5
7	750	450	1	Bagasse	1	0.5	0.5
8	750	500	1	Bagasse	1	0.5	0.5
9	750	400	1	Bagasse	1	0.6	0.5
10	750	400	1	Bagasse	1	0.7	0.5
11	750	400	1	Olive husk	1	0.5	0.5
12	750	400	1	Maple	1	0.5	0.5
13	750	400	1	Oak	1	0.5	0.5
14	750	400	2	Bagasse	1	0.5	0.5
15	750	400	1 + 2	Bagasse	1	0.5	0.5
16	750	400	1	Bagasse	1	0.5	0.75
17	750	400	1	Bagasse	1	0.5	1.0
18	750	400	1	Bagasse	2	0.5	0.5
19	750	400	1	Bagasse	3	0.5	0.5

[a] Standard conditions.

$$M_{\text{tar}} = \int_{\text{reactor}} (\alpha_{\text{g}} \bar{\rho}_{\text{g}} \tilde{Y}_{\text{tar}}) \, \mathrm{d}V, \tag{59}$$

$$M_{\text{feed}} = \int_0^t \int_{\text{inlet}} (\alpha_{\text{b}} \bar{\rho}_{\text{b}} \mathbf{u}_{\text{b}}) \, \mathrm{d}\mathbf{A} \, \mathrm{d}t', \tag{60}$$

where the subscript b denotes biomass. With these definitions, two measures for reactor performance are the yield (η) and the differential reactor efficiency (DRE), ϑ, c.f. Miller and Bellan (1998):

$$\eta_{\text{tar}}(t) = \frac{\Omega_{\text{tar}} + M_{\text{tar}}}{M_{\text{feed}}}, \tag{61}$$

$$\vartheta_{\text{tar}}(t) = \frac{\Omega_{\text{tar}} + M_{\text{tar}}}{\sum_{\xi} (\Omega_{\xi} + M_{\xi})}, \tag{62}$$

where the summation is over the species tar, gas and char. These measures quantify the relative efficiency of reactor tar production relative to the biomass feed flow, and the relative proportion of tar produced compared to gas and char. The above two definitions of tar collection are in fact strongly related. For example, if conditions in the reactor are such that the reaction rate of the pyrolysis is at least equal to the feed rate of biomass to the reactor (i.e. sufficiently high temperature), then both definitions lead to the same steady-state (i.e. states reached at sufficiently long time after reactor start-up) result. Under steady state, mathematically defined by $t \to \infty$, the denominators of Eqs. 61 and 62, M_{feed} and $\sum_{\xi} (\Omega_{\xi} + M_{\xi})$, differ only by a small amount representing the unreacted biomass. Hence the yield and DRE will have the same value, since the unreacted amount of biomass is a negligible term in the limit $t \to \infty$. However, if the pyrolysis rate is lower than the biomass feed rate, as it is under sufficiently low operating temperatures, then the yield will be lower than the DRE. This means that the DRE is an upper limit for the steady-state yield. This relationship between the two collection parameters is important, as it turns out that the DRE reaches a steady-state value earlier than the corresponding yield.

Similar definitions are used for the reactor performance with respect to gas and char production.

4.3.1. Qualitative behavior

To investigate the qualitative behavior of the reactor, snapshots of several variables have been plotted at $t = 1.5$ s, representative for Run No. 3, the standard case.

Fig. 2(a) shows the reactor distribution of the volumetric fraction of the sand and depicts the characteristic void regions present in the bed, which are induced by large-scale instabilities of the mixture. The figure further shows velocity vectors of the sand and gas phases. These indicate (substantiated by snapshots at different times) that the gas motion is preferentially through the void regions where the flow resistance is reduced. Overall, the behavior is similar to that of isothermal beds, as investigated elsewhere (e.g. Lathouwers and Bellan, 2000), in that large recirculating regions are created in the bed. As a result of the fact that the solids volume fraction approaches zero at the top of the bed, the velocity vectors point straight downward, in accordance with the undisturbed slip velocity of a particle. Note, however, that there is no solid mass flux associated with this velocity as the solids volume fraction is low.

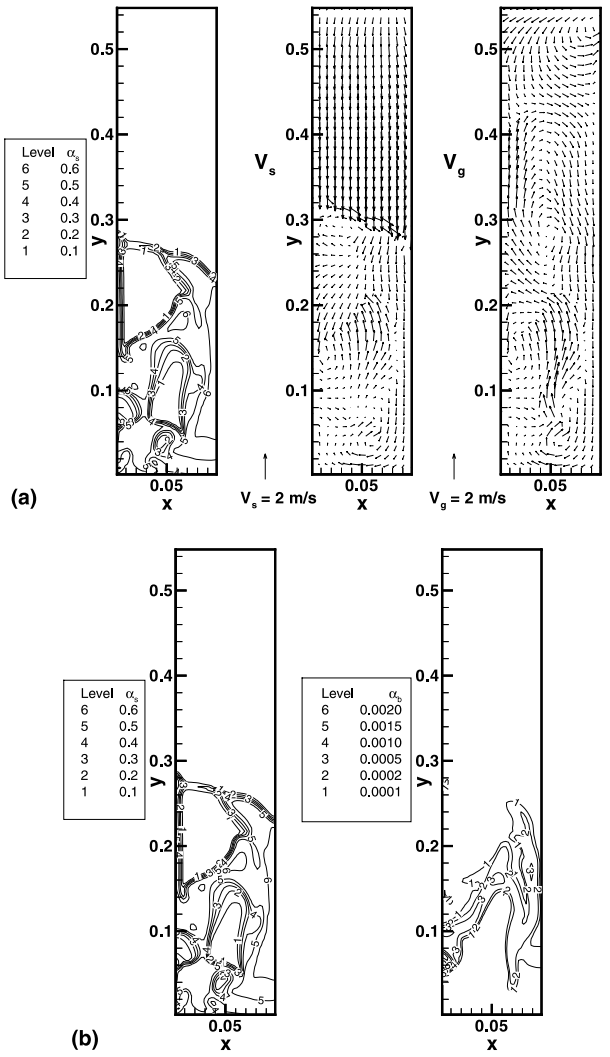

Fig. 2. (a) Volume fraction distribution of solids, carrier gas velocity and solids velocity at $t = 1.5$ s, for Run 3, and (b) volume fraction distribution of sand and biomass at $t = 1.5$ s, for Run 3. The conditions for Run 3 are listed in Table 3.

Displayed in Fig. 2(b) is a comparison of the volume fraction reactor distributions of sand and biomass. Although there are some common qualitative recirculation features, quantitatively the volume fraction of the biomass is generally very small compared to that of the sand, due to the short simulation time. The biomass is relatively evenly distributed over the dense part of the bed, illustrating the effectiveness for solid mixing in fluidized beds.

Plotted in Fig. 3 are reactor distributions of the temperatures of the gas phase, sand, and biomass. Both the gas-phase and sand temperature are almost uniform and equal to the inlet gas-phase temperature (and more importantly, the initial sand temperature), i.e. 750 K. The biomass temperature, however, varies significantly throughout the reactor, showing a distinctive pattern of

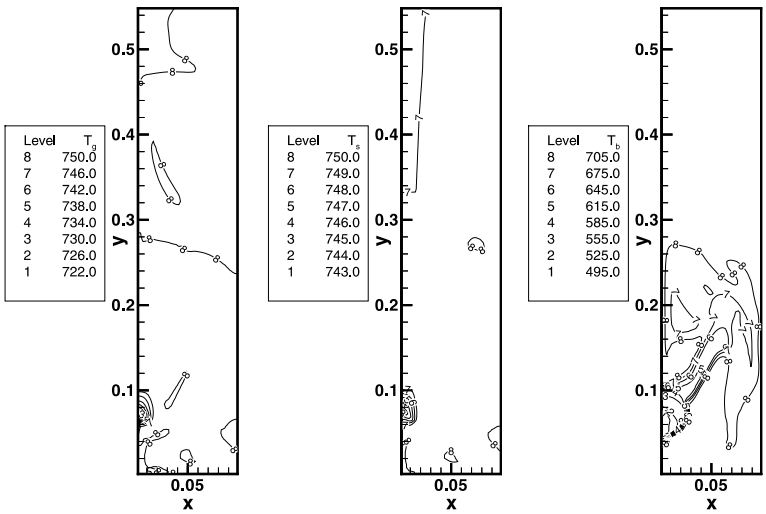

Fig. 3. Temperature distribution of gas, sand and biomass at $t = 1.5$ s, for Run 3 (see Table 3).

biomass entering at the specified feed temperature (400 K), and flowing clockwise while at the same time heating up.

In Fig. 4, the partial macroscopic densities ($= \alpha\rho Y$) of the relevant gas and solid species are illustrated. Therein, biomass refers to the sum of both virgin and active solid components. Both tar and gas densities are high at similar locations representing regions where the biomass temperature has increased enough to produce large quantities of both gaseous products. Although tar originates only from the conversion of the biomass, gas may also be produced from the secondary reaction converting tar to gas (see Eq. 1) in regions of high T_g. Char appears to be most preponderant at locations of low tar and gas production, where the biomass temperature is relatively

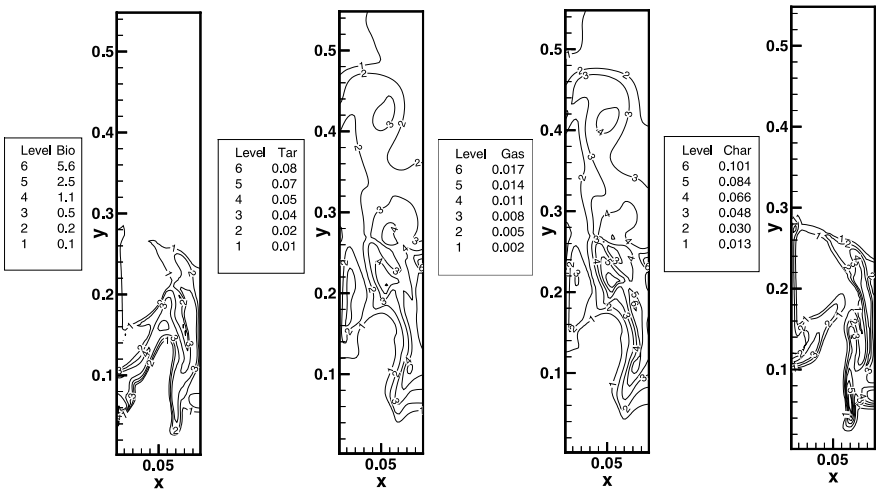

Fig. 4. Partial density distribution of biomass, tar, gas and char at $t = 1.5$ s, for Run 3 (see Table 3).

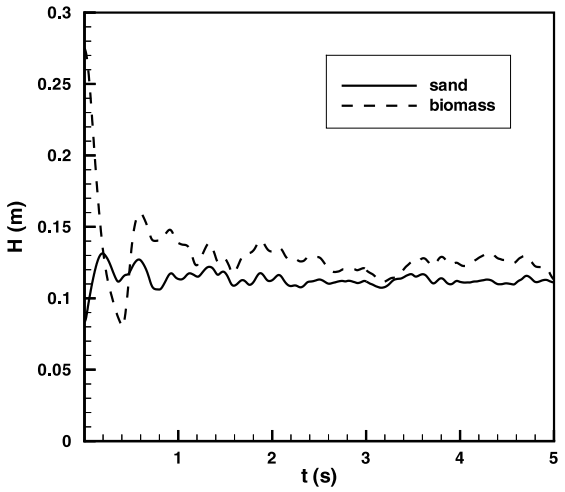

Fig. 5. Averaged vertical coordinate of the sand and biomass center of mass as a function of time for Run 3 (see Table 3).

low (see Fig. 3). For all species, the inhomogeneities in the partial densities are a result of both the inhomogeneous reaction rates and transport processes in the reactor. At later times (not shown), the char distribution becomes more uniform, owing to the effective solid mixing.

To show the particular transient structure due to the bubbling of the bed, the y-coordinate of the sand and biomass center of mass is plotted in Fig. 5 as a function of time. Although both sand and biomass fluctuate in phase, in general, the biomass is situated higher up in the bed than is the sand. This is attributed to both the biomass density being much smaller than that of the sand due to its high porosity, and to the general motion of the biomass which is directed upwards at the feeding point, due to bubbling. By the time the biomass particles move downward, they have already partially pyrolyzed, and those reaching the bottom of the bed contain a substantial amount of unreactive char. This sand/biomass particle segregation may be detrimental to tar production, indicating the need to optimize this yield as a function of reactor and feedstock parameters.

4.3.2. Parametric study

The parametric study is devoted to finding optimum conditions for maximizing tar yield as a function of the relevant operating parameters. The parameters investigated include the temperature of the inlet gas, the feed temperature of the biomass, the particle size, the fluidization velocity (or flux) magnitude, the location of the feed-point(s), and the type of feedstock used for pyrolysis.

Displayed in Figs. 6(a)–(c) are the yields of tar, char and gas, while the corresponding DREs are illustrated in Figs. 7(a)–(c), all as a function of time and for different initial values of T_g. The strong dependence of both yield and DRE on T_g are noteworthy. Comparing the yield with the DRE, it can be concluded that the DRE is a more practical way of examining efficiency than is the yield, which is, however, the quantity of ultimate industrial interest. Both figures indicate that the efficiency of tar production reaches a maximum at $T_g = 750$ K for the

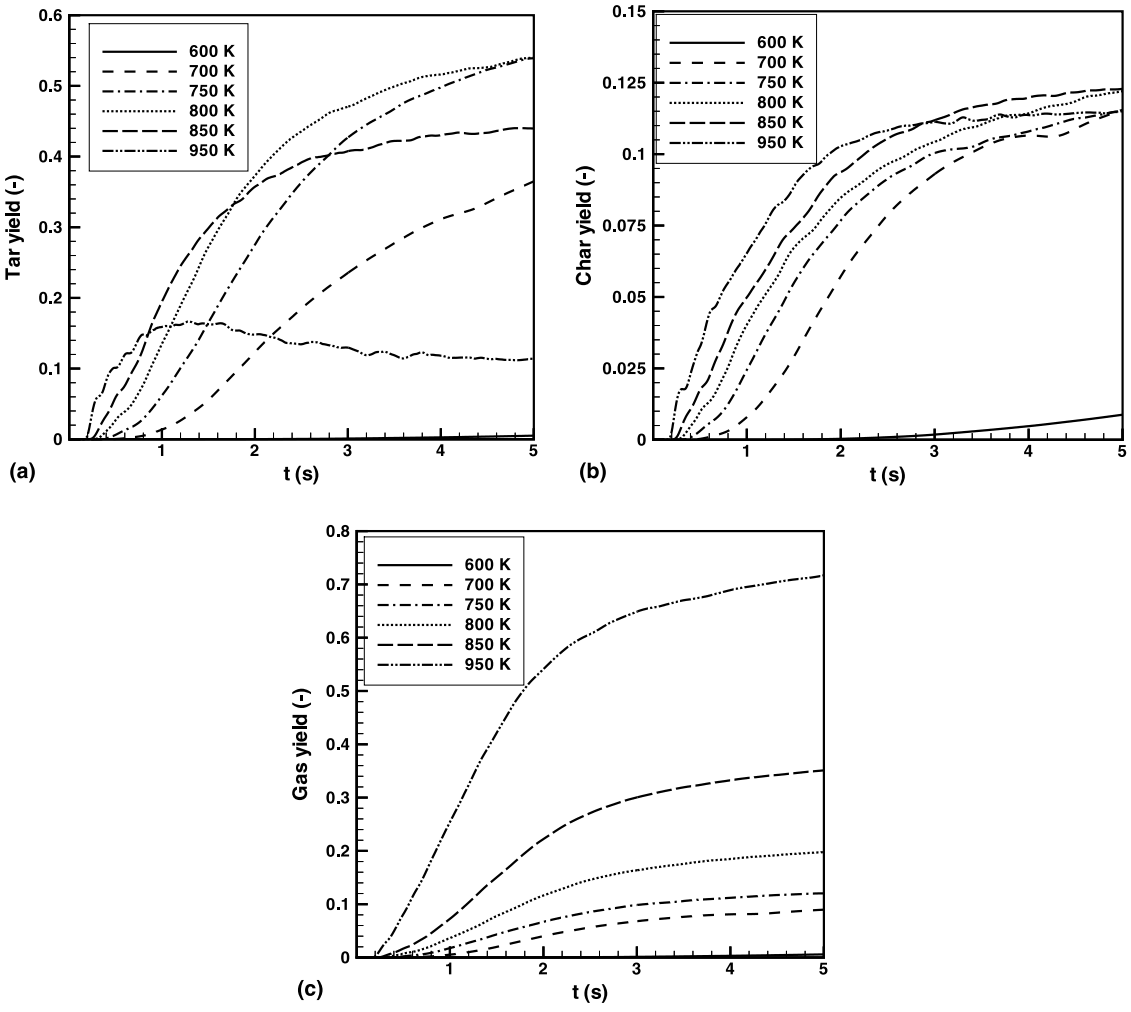

Fig. 6. (a) Tar yield, (b) char yield, and (c) gas yield as a function of time for different fluidization gas temperatures. For detailed simulation conditions see Table 3.

set of discrete temperatures investigated herein. The abrupt decrease in tar DRE at small times corresponds to the large char DRE (see Fig. 7(b)) resulting from the low biomass temperature. However, char yield increases with t (see Fig. 6(b)), as pyrolysis is more vigorous due to increased biomass temperature, whereas the char DRE decreases with increasing t (see Fig. 7(b)), in agreement with the known hindrance of char production at higher reactor temperatures. Moreover, whereas char yield reaches a maximum as a function of the initial T_g (Fig. 6(b)) as the reactions are enhanced at larger temperatures, the DRE continuously decreases as a function of the initial value of T_g (Fig. 7(b)), epitomizing the preponderance of the more efficient conversion to tar as the operating temperature is elevated. Figs. 6(c) and 7(c) show that gas yield continuously increases with time as the biomass temperature becomes larger, but that after the initial transient the gas DRE may either increase or decrease with t, according to the

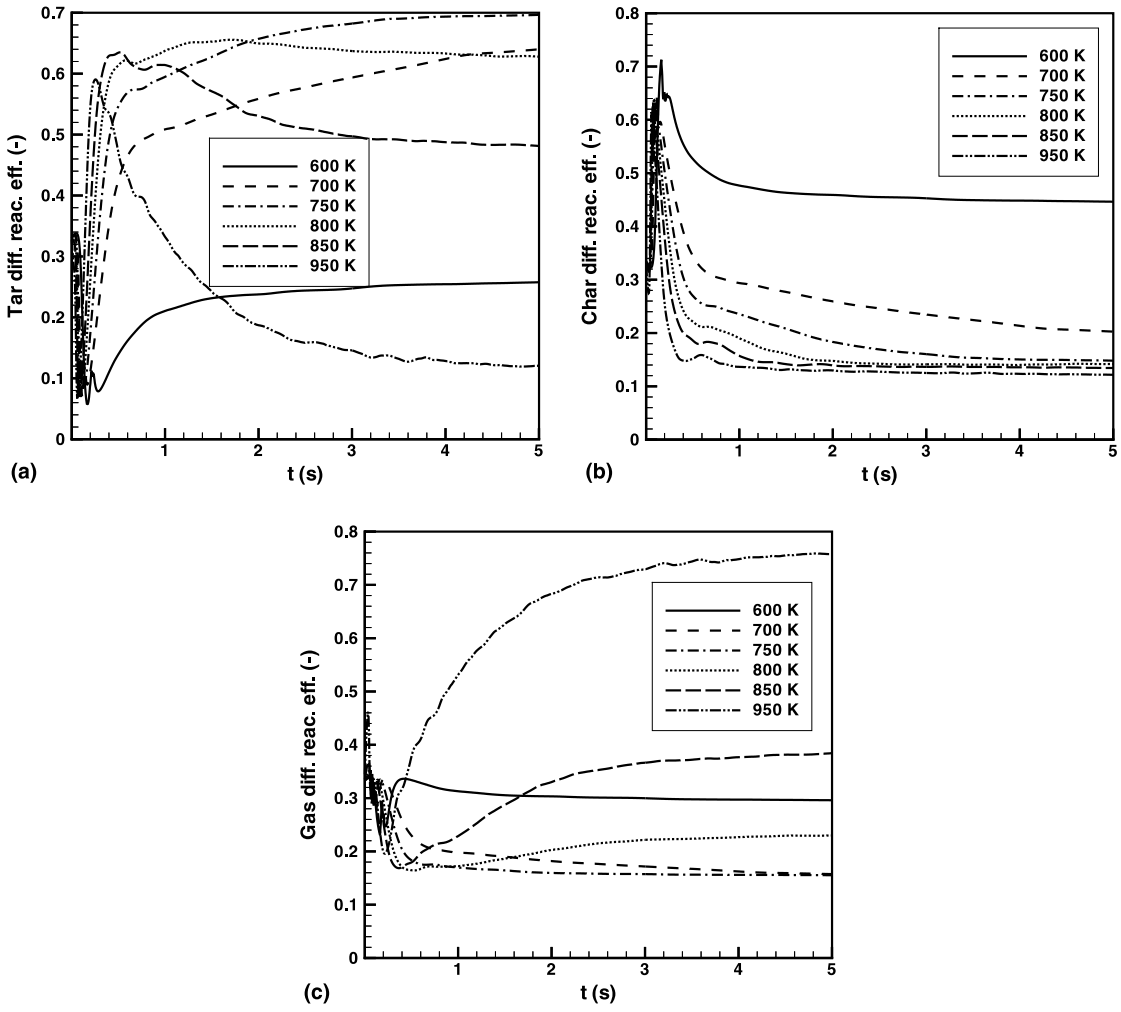

Fig. 7. (a) Tar DRE, (b) char DRE, and (c) gas DRE as a function of time for different fluidization gas temperatures. For detailed simulation conditions see Table 3.

initial temperature. At low temperatures the gas DRE decreases with t, whereas at high temperatures it increases with t owing to the conversion of tar to gas; it is this unwanted conversion that must be mitigated in industrial reactors to obtain a commercially viable system. In fact, the gas DRE seems to be minimized for $T_g = 750$ K, indicating that this is the most likely optimal temperature for maximizing tar yield for the set of discrete temperatures investigated herein. The general observation is that the tar DRE is reduced by the large char DRE at small T_g, whereas at large T_g the tar DRE is reduced by the large gas DRE (see Fig. 7(c)).

To further understand why tar collection is maximized at 750 K, consider the ratio of the characteristic time for tar decomposition, τ_{tar}, to the mean tar residence time, τ_R. The first time scale is estimated from the corresponding Arrhenius reaction rate K_4 in Table 1, while a measure

of the characteristic tar residence time is the mean residence time of the fluidization gas. Therefore, this ratio is

$$\frac{\tau_R}{\tau_{tar}} = \frac{L_y}{V_g} A_{tar} \exp(-E_{tar}/R_u T_g), \tag{63}$$

where L_y is the height of the reactor (see Fig. 1), and V_g is the fluidization velocity (see Table 3). Depicted in Fig. 8 is the ratio displayed in Eq. 63, calculated for $L_y = 0.55$ m and $V_g = 0.5$ m/s, and in the range $T_g = 650$–950 K. For all T_g for which $\tau_R \ll \tau_{tar}$, the formed tar is not converted to gas before leaving the reactor. If one considers that the threshold for minimal tar conversion is $\tau_R/\tau_{tar} \sim 0.1$, then the corresponding T_g from Fig. 8 is 740 K. Since an ideal reactor should operate at as high as possible temperature (to maximize tar formation) while minimizing tar-to-gas conversion, the optimum $T_g = 750$ K found in Fig. 6 from a set of discrete-temperature simulations is totally consistent with the simple estimate obtained from Eq. 63.

Illustrated in Figs. 9(a)–(e) is the effect of different operating conditions on the tar yield. Figs. 9(a), (b) and (c) show the effects of variations in biomass feed temperature, fluidization gas flux magnitude, and the biomass injection point, respectively, on the tar yield. The results show that the changes in these parameters cause only minor variations in the tar yield. The results should be interpreted accounting for the assumption of no pyrolysis before entering the reactor and uniform particle temperature (kinetically controlled regime).

Fig. 9(d) shows the effect of employing different biomass types as feedstock. Bagasse returns the highest tar yield due to the largest proportion of cellulose and the smallest proportion of lignin present in this feed; however its DRE is lowest due to the largest gas DRE (both not shown). Basically, the formed tar decomposes to gas before it can be collected. This points out to the higher-than-optimal fluidizing gas temperature for this case. At the opposite end of the spectrum is olive husk, having considerably higher lignin content and producing the least

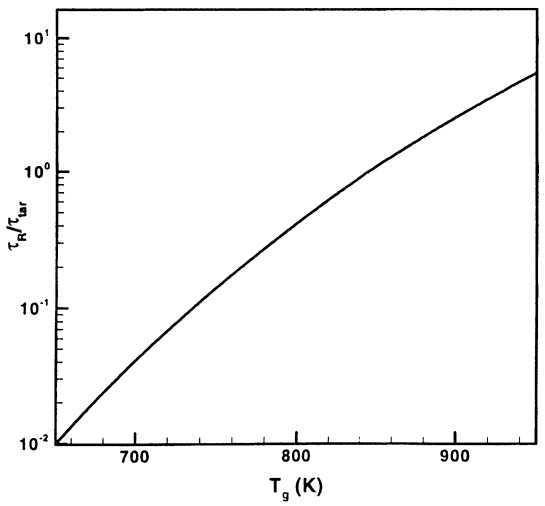

Fig. 8. Ratio of the mean tar residence time to the tar-to-gas conversion kinetic time as a function of fluidization gas temperatures.

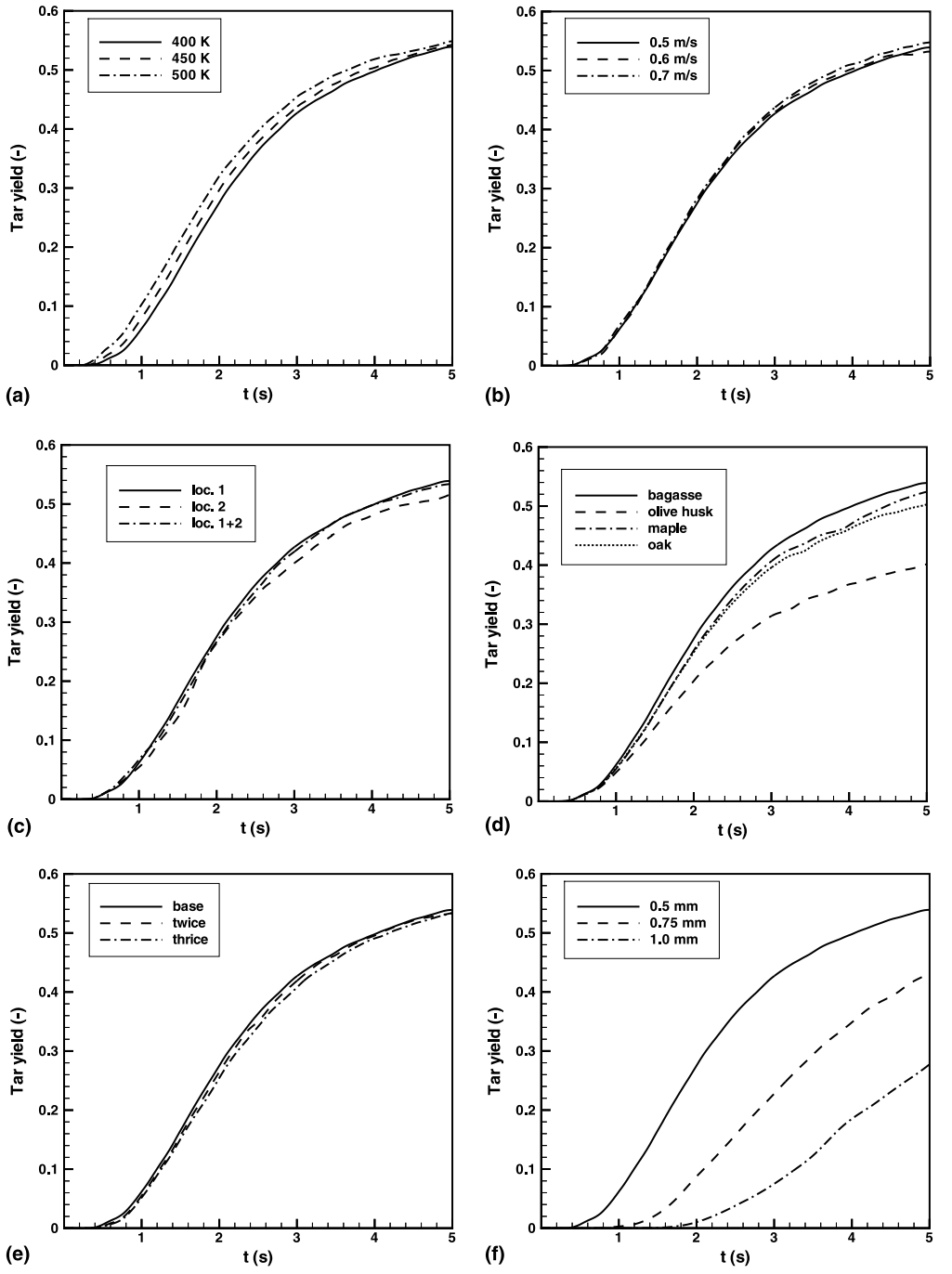

Fig. 9. Tar yield as a function of time for different (a) biomass injection temperatures, (b) fluidization fluxes, (c) biomass injection locations, (d) biomass feedstock, (e) biomass feed rates, and (f) biomass particle sizes. For detailed simulation conditions see Table 3.

collectible tar. Between these two extreme values, the ordering of tar yield is a decreasing function of the percentage of lignin rather than an increasing function of the percentage of cellulose. This indicates that char formation together with tar conversion to gas contribute to the reduced collectible tar.

The effect of the feed rate of biomass is depicted in Fig. 9(e). Increasing the feed rate has no distinctive effect on the yield. This indicates that the characteristic time of tar formation is the largest, and this is therefore the slowest mechanism which then dominates the entire tar production process. This is an important observation for system scale-up in that, as discussed above, the DRE is the appropriate measure of the steady-state yield when the reactor runs at maximum feed rate. Finally, Fig. 9(f) shows the effect of using different particle diameters on the tar yield. Increasing the particle diameter by a factor of 1.5 or 2 leads to a significant reduction in yield, at least on this time scale; this reduction is associated with an increased particle heat-up time.

5. Conclusions

A comprehensive mathematical model has been derived that is capable of predicting the thermofluid dynamics of dense reacting gas–solid mixtures. The model is based on a multiphase description obtained from systematic averaging of the local instantaneous equations using the kinetic theory of granular flows in combination with rigid sphere interaction models explicitly accounting for collisional transfer. Multiple solid classes are considered to enable a differentiation in either physical properties or thermochemical behavior of various particle types, e.g. fuel versus inert particles. Separate transport equations are used for each particle class, allowing for the independent acceleration of the particles in each class and non-equilibrium processes leading to momentum and energy exchange between respective classes, and between particles and the carrier gas. The model avoids heuristic extensions from monodisperse results that are common in literature. To illustrate this general gas–solid reacting model, simulations are conducted for biomass pyrolysis in a fluidized bed. In this specific case, a previously validated, chemistry model for biomass particle pyrolysis (seven solid species, two gaseous species), capable of differentiating between different feedstocks, is coupled to the hydrodynamics formulation.

The model has been applied to high-temperature particle pyrolysis in a lab-scale fluidized bed reactor for which a parametric study has been performed. At fixed initial biomass particle size, the major operating parameter determining the tar yield is the temperature of the fluidization gas. For the discrete values of fluidizing gas temperature used in the simulations, an optimum yield was found for 750 K. Parametric variations in other process parameters, such as fluidization flux magnitude, biomass feed temperature, and feed position, were found to be of relatively minor importance, while the particle size had considerable impact on the tar yield on the time scale of the simulations.

The results of this comparison further indicate that the model captures the key features of the pyrolysis process, and is general enough to be used for the optimization of reactor geometries and operating parameters, such as gas temperature, biomass injection procedures, etc. The model is thus used elsewhere (Lathouwers and Bellan, 2001) to optimize and scale up a biomass pyrolysis reactor.

Acknowledgements

The authors would like to thank Profs. L.I. Zaichik and L.A. Dombrovsky of the Institute for High Temperatures, Moscow, Russia, for discussions on radiation modeling. This research was conducted at the Jet Propulsion Laboratory (JPL) and sponsored by the US Department of Energy (DOE), with Mr. Neil Rossmeisel (DOE Headquarters) and Mr. D. Hooker (DOE Golden Center) serving as contract monitors, under an agreement with the National Aeronautics and Space Administration. Computational resources were provided by the supercomputing facility at JPL.

Appendix A. Derivation of the self-diffusion coefficient

The diffusive flux associated with fluctuations in particle velocity and a variable Ψ is $-\nabla\cdot(\alpha_i\bar{\rho}_i\langle\mathbf{C}_i\Psi_i'\rangle)$. As the distribution for Ψ is unknown, we use mean free path theory to obtain a reasonable estimate of this flux (Chapman and Cowling, 1970). Following Chapman and Cowling we have $-\langle\mathbf{C}_i\Psi_i'\rangle\approx 1/2\bar{C}_i l_i\nabla\Psi_i$, where $\bar{C}_i$ is the average magnitude of C_i and l_i denotes the mean free path of particles in class i. Comparing this formulation with the original flux, we deduce the diffusion coefficient as $\mathscr{D}_{ii}=1/2\bar{C}_i l_i$. For a Gaussian distribution, the average magnitude of the fluctuating velocity is $\bar{C}_i=(8\Theta_i/\pi)^{1/2}$. The mean free path for a particle of class i is given by (Chapman and Cowling, 1970) $l_i=n_i\bar{C}_i/\sum_k N_{ik}$, where the collision frequencies N_{ik} are given by $N_{ik}=n_i n_k h_{ik}\sigma_{ik}^2\sqrt{8\pi(\Theta_i+\Theta_k)}$ in the low drift limit. For a dilute gas ($h_{ik}=1$) at equilibrium conditions, the classical expression given by Chapman and Cowling (1970) is recovered. The above diffusion coefficient is only valid when the dynamics of the particle evolves relatively slowly between collisions, i.e. $\mathrm{d}\Psi/\mathrm{d}t\approx 0$, i.e. the time scale for collisions is much smaller than a characteristic time scale for particle dynamics. For dense systems, this condition is likely to be satisfied. Hsiau (2000) recently presented an analysis for heat conduction in granular flows where this assumption is relaxed. At sufficiently low volume fractions, the mean free path becomes comparable with the size of the vessel and the diffusion coefficient is heuristically corrected to prevent unrealistically large diffusion (c.f. Louge et al., 1993), $\mathscr{D}_{ii}^*=\mathscr{D}_{ii}/(1+l_i/L)$, where L is a measure of the vessel size taken as the maximum of the x- and y-directional sizes.

References

Anderson, K.G., Jackson, R., 1992. A comparison of the solutions of some proposed equations of motion of granular materials for fully developed flow down inclined planes. J. Fluid Mech. 241, 145–168.

Balzer, G., Boelle, A., Simonin, O., 1995. Eulerian gas–solid flow modelling of dense fluidized bed. In: FLUIDIZATION VIII, Proceedings of the International Symposium of the Engineering Foundation. pp. 1125–1134.

Barrett, R., Berry, M., Chan, T.F., Demmel, J., Donato, J., Dongarra, J., Eijkhout, V., Pozo, R., Romine, C., Van der Vorst, H., 1994. Templates for the Solution of Linear Systems: Building Blocks for Iterative Methods. SIAM, Philadelphia.

Brown, P.N., Byrne, G.D., Hindmarsh, A.C., 1989. VODE: a Variable-coefficient ODE solver. SIAM J. Sci. Stat. Comput. 10, 1038–1051.

Campbell, C.S., 1990. Rapid granular flows. Annu. Rev. Fluid Mech. 22, 57–92.
Campbell, C.S., Wang, D.G., 1991. Particle pressure in gas-fluidized beds. J. Fluid Mech. 227, 495–508.
Chapman, S., Cowling, T.G., 1970. The Mathematical Theory of Nonuniform Gases. Cambridge University Press, Cambridge.
Di Felice, R., Coppola, G., Rapagna, S., Jand, N., 1999. Modeling of biomass devolatilization in a fluidized bed reactor. Can. J. Chem. Eng. 77, 325–332.
Drew, D.A., 1983. Mathematical modeling of two-phase flow. Annu. Rev. Fluid Mech. 15, 261–291.
Farell, M., Lun, C.K.K., Savage, S.B., 1986. A simple kinetic theory for granular flow of binary mixtures of smooth, inelastic, spherical particles. Acta Mech. 63, 45–60.
Gidaspow, D., 1986. Hydrodynamics of fluidization and heat transfer: supercomputer modelling. Appl. Mech. Rev. 39, 1–22.
Goldhirsch, I., 1999. Scales and kinetics of granular flows. Chaos 9, 659–672.
Goldman, E., Sirovich, L., 1967. Equations for gas mixtures. Phys. Fluids 10, 1928–1940.
Gourdel, C., Simonin, O., Brunier, E., 1999. Two-Maxwellian equilibrium distribution function for the modelling of a binary mixture of particles. In: Werther, J. (Ed.), Circulating Fluidized Bed Technology VI, Proc. of the 6th Int. Conference on Circulating Fluidized Beds. DECHEMA, Frankfurt am Main, Germany, pp. 205–210.
Gyarmathy, G., 1982. The spherical droplet in gaseous carrier streams: review and synthesis. In: Hewitt, G.F., Delhaye, J.M., Zuber, N. (Eds.), Multiphase Science and Technology, vol. 1. McGraw-Hill, New York, pp. 99–279.
Hsiau, S.S., 2000. Effective thermal conductivities of a single species and a binary mixture of granular materials. Int. J. Multiphase Flow, 387–419.
Jenkins, J.T., Mancini, F., 1987. Balance laws and constitutive relations for plane flows of a dense, binary mixture of smooth, nearly elastic, circular disks. J. Appl. Mech. 54, 27–34.
Jenkins, J.T., Mancini, F., 1989. Kinetic theory for binary mixtures of smooth, nearly elastic spheres. Phys. Fluids A 1, 2050–2057.
Jenkins, J.T., Richman, M.W., 1985. Grad's 13-moment system for a dense gas of inelastic spheres. Arch. Ration. Mech. Anal. 87, 355–377.
Jenkins, J.T., Savage, S.B., 1983. A theory for the rapid flow of identical, smooth, nearly elastic, spherical particles. J. Fluid Mech. 130, 187–202.
Johnsson, F., Anderson, S., Leckner, B., 1991. Expansion of a freely bubbling fluidized bed. Powder Technol. 68, 117–123.
Johnson, P.C., Jackson, R., 1987. Frictional–collisional constitutive relations for granular materials, with application to plane shearing. J. Fluid Mech. 176, 67–93.
Kumaran, V., Koch, D.L., 1993a. Properties of a bidisperse particle–gas suspension. Part 1. Collision time small compared with viscous relaxation time. J. Fluid. Mech. 247, 623–641.
Kumaran, V., Koch, D.L., 1993b. Properties of a bidisperse particle–gas suspension. Part 2. Viscous relaxation time small compared with collision time. J. Fluid. Mech. 247, 643–660.
Lathouwers, D., 1999. Modelling and simulation of turbulent bubbly flows. Ph.D. thesis, Delft University of Technology, The Netherlands.
Lathouwers, D., Bellan, J., 2000. Modeling and simulation of bubbling fluidized beds containing particle mixtures. Proc. Combust. Inst. 28, 2297–2304.
Lathouwers, D., Bellan, J., 2001. Yield optimization and scaling of fluidized beds for tar production from biomass. Energy & Fuels 15, 1247–1262.
Louge, M., Yusof, J.M., Jenkins, J.T., 1993. Heat transfer in the pneumatic transport of massive particles. Int. J. Heat Mass Transfer 36, 265–275.
Lun, C.K.K., Savage, S.B., Jeffrey, D.J., Chepurniy, N., 1984. Kinetic theories for granular flow: inelastic particles in Couette flow and slightly inelastic particles in a general flow field. J. Fluid Mech. 140, 223–256.
Manger, E., 1996. Modelling and simulation of gas/solids flow in curvilinear coordinates. Ph.D. thesis, Telemark College, Norway.
Miller, R.S., Bellan, J., 1997. A generalized biomass pyrolysis model based on superimposed cellulose, hemicellulose and lignin kinetics. Combust. Sci. Technol. 126, 97–137.

Miller, R.S., Bellan, J., 1998. Numerical simulation of vortex pyrolysis reactors for condensable tar production from biomass. Energy & Fuels 12, 25–40.

Miller, R.S., Harstad, K., Bellan, J., 1999. Evaluation of equilibrium and non-equilibrium evaporation models for many-droplet gas–liquid flow simulations. Int. J. Multiphase Flow 24, 1025–1055.

Savage, S.B., Sayed, M., 1984. Stresses developed by dry cohesionless granular materials sheared in an annular shear cell. J. Fluid Mech. 142, 391–430.

Schiller, L., Nauman, A., 1935. A drag coefficient correlation. VDI Zeitung 77, 318–320.

Scott, D.S., Majerski, P., Piskorz, J., Radlein, D., 1999. A second look at fast pyrolysis of biomass – the RTI process. J. Anal. Appl. Pyrol. 51, 23–37.

Scott, D.S., Piskorz, J., 1982. The flash pyrolysis of aspen-poplar wood. Can. J. Chem. Eng. 60, 666–674.

Scott, D.S., Piskorz, J., 1984. The continuous pyrolysis of biomass. Can. J. Chem. Eng. 62, 404–412.

Syamlal, M., 1993. MFIX documentation theory guide. DOE report no. DOE/METC-94/1004.

Sun, J., Chen, M.M., 1988. A theoretical analysis of heat transfer due to particle impact. Int. J. Heat Mass Transfer 31 (5), 969–975.

Tham, M.K., Gubbins, K.E., 1971. Kinetic theory of multicomponent dense fluid mixtures of rigid spheres. J. Chem. Phys. 55, 268–279.

Valiveti, P., Koch, D.L., 1998. Instability of sedimenting bidisperse particle gas suspensions. Appl. Sci. Res. 58, 275–303.

Zaichik, L.I., Pershukov, V.A., Kozelev, M.V., Vinberg, A.A., 1997. Modeling of dynamics, heat transfer, and combustion in two-phase turbulent flows: 2. Flows with heat transfer and combustion. Exp. Therm. Fluid Sci. 15, 311–322.

Zamankhan, P., 1995. Kinetic theory of multicomponent dense mixtures of slightly inelastic spherical particles. Phys. Rev. E 52, 4877–4891.